Phosphoproteomic identification of Mos-MAPK targets in meiotic cell cycle and asymmetric oocyte divisions

Ivan Avilov[1], Yehor Horokhovskyi[2], Pooja Mehta[1], Luisa Welp[3], Jasmin Jakobi[1], Mingfang Cai[1], Aleksander Orzechowski[1], Henning Urlaub[3,4], Juliane Liepe[2] and Peter Lenart[1]

[1]Research Group Cytoskeletal Dynamics in Oocytes, [2]Research Group Quantitative and Systems Biology, and [3]Research Group Bioanalytical Mass Spectrometry, Max Planck Institute for Multidisciplinary Sciences, Am Fassberg 11, 37077, Göttingen, Germany;

[4]Cluster of Excellence "Multiscale Bioimaging: from Molecular Machines to Networks of Excitable Cells" (MBExC), University of Göttingen, D-37075 Göttingen, Germany

Running title: Phosphoproteomics identifies targets of Mos-MAPK

Correspondence to peter.lenart@mpinat.mpg.de

Abstract

The Mos kinase activates the ERK/MAPK pathway during oocyte meiosis, controlling essential meiotic functions in species across metazoa. However, despite its significance, the molecular targets of Mos-MAPK remain largely unidentified. Here, we addressed this question using starfish oocytes ideally suited to combine cellular assays with phosphoproteomics. This revealed CPE-mediated mRNA polyadenylation as a prominent target of Mos-MAPK, and we show that translation is required to drive the second meiotic division. Secondly, we identify a well-defined subset of cytoskeletal regulators as targets of Mos-MAPK. We show that this regulation is critical to ensure the asymmetry of meiotic divisions primarily by reducing the growth of astral microtubules. This allows positioning of the spindle directly beneath the cortex and prevents the separation of spindle poles in anaphase, thereby minimizing polar body size. Thus, by phosphoproteomics we reveal molecular modules controlled by Mos-MAPK explaining how this single, conserved kinase can act as a switch between the mitotic and meiotic division programs.

Introduction

Oocyte meiosis is a specialized form of cell division adapted to produce the fertilizable egg. This is achieved through two highly asymmetric divisions, meiosis I (MI) and meiosis II (MII), without an intervening S-phase, resulting in a single, large, haploid egg and small unviable polar bodies as byproducts (Mullen et al., 2019; Jessus et al., 2020). Strikingly, after fertilization, in the same egg cytoplasm embryonic mitoses take place with alternating S- and M-phases showing typical mitotic and lacking meiosis-specific features. What mediates this dramatic switch between meiotic and mitotic division programs?

The Mos kinase is a constitutive activator of the ERK/MAPK cascade that is present during oocyte meiosis, and is degraded after fertilization (Dupré et al., 2010). Therefore, the ERK/MAPK pathway and the downstream effector $p90^{RSK}$ are active during oocyte meiosis, but not in mitosis. That this peculiar Mos-MAPK activity plays critical roles in driving the meiotic division program has been shown in species across metazoa: first in *Xenopus* oocytes (Sagata et al., 1988), followed by studies in mice (Colledge et al., 1994; Hashimoto et al., 1994), starfish (Tachibana et al., 2000), tunicates (Sensui et al., 2012), and in cnidarian jellyfish (Amiel et al., 2009). In some of these species, Mos-MAPK is required for triggering meiotic maturation (Sagata et al., 1988), however a more widely conserved function of Mos-MAPK appears to be preventing S-phase between MI and MII, and driving oocytes directly into MII. Mos-MAPK inhibition causes oocytes to reform the nucleus and initiate S-phase after MI in *Xenopus* and starfish oocytes (Sagata et al., 1988; Tachibana et al., 2000), and mouse oocytes also display signs of meiotic exit after MI (Araki et al., 1996; Phillips et al., 2002; Verlhac et al., 1996). An even more prominent function of Mos is to establish the 'cytostatic factor (CSF) arrest', i.e. to halt meiosis until fertilization, and thereby synchronize these two vital processes (Jessus et al., 2020). Across species, Mos-MAPK inhibition leads to the loss of CSF arrest and parthenogenetic activation of oocytes (Sagata et al., 1988; Colledge et al., 1994; Hashimoto et al., 1994; Tachibana et al., 2000; Mori et al., 2006). Common to these seemingly unrelated functions is that they directly or indirectly involve increasing or sustaining Cdk1-Cyclin B activity. While in most species the detailed mechanisms remain unclear, it is well understood in *Xenopus* oocytes that Mos-MAPK facilitates Cyclin B translation to trigger meiotic maturation and to drive MII (Abrieu et al., 2001; Hochegger et al., 2001). Furthermore, for maintenance of the CSF arrest, degradation of Cyclin B is prevented by phosphorylation of Erp1/Emi2 by $p90^{RSK}$ downstream of Mos-MAPK (Wu and Kornbluth, 2008; Isoda et al., 2011).

Besides meiosis-specific cell cycle regulation, Mos-MAPK activity is also required for the asymmetric meiotic divisions. From jellyfish through starfish to mice, Mos-MAPK inhibition alters

meiotic spindle morphology converting them to somewhat 'mitotic-like' displaying long, astral-like microtubules. This interferes with asymmetric division resulting in enlarged polar bodies or failed polar body cytokinesis (Araki et al., 1996; Verlhac et al., 1996; Bodart et al., 2002; Amiel et al., 2009; Ucar et al., 2013). The reverse effect has also been observed in tunicates: mitotic embryos ectopically expressing Mos show short, meiotic-like spindles and extrude polar bodies (Dumollard et al., 2011). In mouse oocytes, two spindle regulators under the control of Mos-MAPK, MISS and DOC1R have been identified and characterized in substantial detail (Lefebvre et al., 2002; Terret et al., 2003). However, a mechanistic model of how Mos-MAPK regulates spindle organization is lacking.

Here, we took advantage of starfish oocytes that are transparent, synchronous and available in large quantities to identify downstream targets of Mos-MAPK by quantitative phosphoproteomics. We used imaging assays to characterize cellular phenotypes of Mos-MAPK inhibition in live oocytes, and then analyzed samples by phosphoproteomics precisely timed to key transitions. This revealed conserved molecular modules under the control of Mos-MAPK explaining how Mos-MAPK activity may drive the meiotic division program.

Results and discussion

Mos-MAPK drives the second meiotic division

First, we confirmed earlier observations by Tachibana and coworkers (Tachibana et al., 2000; Ucar et al., 2013) showing that the Mos kinase activates the ERK/MAPK pathway specifically during meiosis, not active in immature oocytes and inactivated again at the end of MII (Fig. 1A). This activity is effectively and specifically inhibited by 20 μM of the small-molecule MEK inhibitor, U0126 without interfering with hormone-induced maturation and the initial activation of Cdk1-cyclin B leading up to nuclear envelope breakdown (NEBD) (Fig. 1A, S1A, B).

We then imaged live oocytes by high-resolution confocal microscopy to complement previous, detailed biochemical characterization of Mos-MAPK inhibition (Tachibana et al., 2000; Mori et al., 2006). After NEBD, chromosomes congressed to the animal pole both in U0126- and DMSO-treated oocytes and the MI spindle formed with normal timing, indicating that these early steps of meiosis are independent of Mos-MAPK (Fig. 1B, C). However, at metaphase the MI spindle showed a slightly enlarged morphology and the polar bodies were consistently larger in U0126-treated oocytes (Fig. 1B, S1C-E and see below). Additionally, while DMSO-treated oocytes rapidly progressed to MII, forming the MII spindle within ~30 minutes, U0126-treated oocytes failed to transition to MII (Fig.

1B). Unlike control oocytes, in which chromosomes remained condensed and the nuclear envelope did not re-form during the MI-MII transition, U0126-treated oocytes exited meiosis after MI evidenced by decondensation of chromatin and reformation of the nucleus (Fig. 1B, E). Even in absence of fertilization, U0126-treated oocytes then initiated the first mitotic division and began parthenogenetic embryo development with similar timing to untreated and fertilized oocytes (Fig. 1B, D). The, counting from the start of meiosis, second metaphase spindle in U0126-treated oocytes showed a morphology very similar to control mitotic spindles, about twice larger in length and centrosomal area size than meiotic spindles (Fig. S1C-E).

In *Xenopus,* S-phase is prevented between MI and MII by rapid reactivation of Cdk1-Cyclin B, forcing direct entry into MII (Gerhart et al., 1984). This results from translation of Cyclin B protein and activatory dephosphorylation of Cdk1 shortly after completion of MI (Hochegger et al., 2001; Iwabuchi et al., 2000). To test whether in starfish oocytes active Cdk1-Cyclin B is sufficient to rescue the effect of Mos-MAPK inhibition, we injected oocytes with active Cdk1-Cyclin B protein shortly after metaphase I (Fig. 1F). This treatment reversed the effect of Mos-MAPK inhibition: while U0126-treated oocytes exited MI, formed a pronucleus and entered parthenogenetic development, Cdk1-Cyclin B injected oocytes assembled an MII spindle without forming a pronucleus (Fig. 1F). MII spindles in these Cdk1-Cyclin B-injected oocytes showed a meiotic morphology, unlike the mitotic-like morphology in U0126-treated oocytes.

Taken together, consistent with previously published biochemical data, we show that in starfish oocytes Mos-MAPK is activated after NEBD, and its inhibition has no effect on maturation and spindle assembly before the metaphase of MI. However, soon after Mos-MAPK is activated, phenotypes of Mos-MAPK inhibition become evident: the metaphase I spindle is enlarged resulting in the formation of an enlarged polar body. Subsequently, Mos-MAPK inhibition prevents reactivation of Cdk1-Cyclin B after MI that would normally drive transition to MII. Therefore, Mos-MAPK inhibited oocytes exit the meiotic program after MI and proceed to parthenogenetic development while skipping MII completely.

Mapping downstream targets of Mos-MAPK by phosphoproteomics

Based on the above observations and taking advantage of the high synchronicity of starfish oocytes, we collected samples for phosphoproteomics at the metaphase of MI; soon after Mos-MAPK is activated, and as soon as the first cellular phenotypes of Mos-MAPK inhibition are evident. Thereby we expect to identify mostly direct effects. Oocytes were collected from three starfish animals, each

136 treated with U0126 or an equal amount of DMSO and then matured (Fig 2A). Synchronicity was
137 confirmed by staining a small portion of the sample with Hoechst 33342 that showed 92-96%
138 metaphase figures. Samples were then enriched for phosphopeptides and analyzed by multiplexed
139 quantitative tandem mass tag (TMT) mass spectrometry identifying 9,035 protein groups, of which
140 3,197 contained phosphopeptides (see Source Data File 1 for complete dataset).

141 We then used ratios of phosphorylated peptides to their total protein intensities in U0126- *vs.*
142 DMSO-treated samples (of 14,360 phospho-peptides identified, 10,880 unique phospho-peptides
143 and 16,621 sequence-PTM combinations were quantified). This resulted in 211 unique phospho-
144 peptides (205 down-, 6 upregulated, 360 sequence-PTM combinations) that passed significance
145 threshold (Source Data File 3). Unsupervised clustering clearly separated U0126-treated samples
146 from DMSO controls, evidencing an effect much above biological variability despite sampling
147 genetically diverse individuals (Fig. 2B).

148 Next, we performed an over-representation analysis revealing the enrichment of gene ontology
149 (GO) terms related to cell cycle and cytoskeletal regulation among the dephosphorylated proteins
150 (Fig. 2C). We also predicted putative human protein kinases corresponding to the observed de-
151 phosphorylation activity (Johnson et al., 2023). This showed an enrichment of kinases of the MAPK-
152 pathway (STE kinase family) and its downstream effector $p90^{RSK}$ (AGC kinase family) (Fig. 2D).
153 Analysis of the predicted upstream kinases revealed that the Mos-MAPK-$p90^{RSK}$ pathway had one of
154 the largest sets of peptide targets and highest predicted ranks, followed by putative targets of Cdk1
155 (Fig. S2A).

156 We complemented the phosphoproteomics experiment at metaphase of MI with a DIA (Data
157 Independent Acquisition) proteomics experiment to monitor changes in protein levels at
158 subsequent stages (Fig. 2E, see Source Data File 2 for complete dataset). In this experiment we were
159 able to identify 7,480 protein groups of which 5,103 protein groups could be quantified. This
160 dataset did not reveal major overall changes in protein abundance consistent with previous work
161 by Swartz *et al.* showing that the proteome is largely stable during meiosis in starfish oocytes (Fig.
162 2F) (Swartz et al., 2021). However, they showed that a very limited subset of proteins, including key
163 cell cycle regulators, do change in abundance that we were able to recapitulate in our time course
164 experiment (Fig. 2G and S2B and see discussion below).

165

166 *Phosphoproteomics identifies functional modules downstream of Mos-MAPK*

167 We then displayed the differentially phosphorylated peptides on a volcano plot, and manually
168 annotated these hits to identify functional modules (Fig. 3A, B, Table S1 and Source Data File 3).

169 In the U0126-treated samples, we detected dephosphorylation of MEK and the downstream effector
170 $p90^{RSK}$, consistent with effective inhibition of the Mos-MAPK pathway. Additionally, we found
171 several components of the core cell cycle machinery to be differentially dephosphorylated,
172 including the Cdc25 phosphatase, the Myt1 kinase, the APC/C subunit Cdc27 (APC3), as well as
173 Arpp19 and PP2A. These changes indicate that Mos-MAPK inhibition acts towards Cdk1-Cyclin B
174 inactivation, suggesting that normally Mos-MAPK activity contributes to keep Cdk1 activity high to
175 allow rapid transition to MII -- fully consistent with our findings above.

176 Manual annotation revealed translational regulation as another prominent functional module
177 downstream of Mos-MAPK. This was not immediately apparent in the GO-term enrichment analysis,
178 as we only identified a specific subset of 11 out of the 1,059 proteins associated with the broad
179 term "translation". These proteins are components of the CPE-mediated mRNA polyadenylation
180 pathway that is known to have critical importance in oocytes documented extensively in *Xenopus* as
181 well as in other model systems (Conti and Kunitomi, 2024; Richter and Lasko, 2011; Mendez and
182 Richter, 2001; Piqué et al., 2008). CPEB binds to the CPE element in the 3'UTR of transcripts and
183 forms both repressive complexes that prevent translation and the active complex that facilitates
184 translation by polyadenylation of the mRNA. During oocyte maturation, CPEB is thought to be first
185 phosphorylated by Aurora A and then hyper-phosphorylated by Cdk1 and Mos-MAPK. These
186 phosphorylations are required for the formation of the active complex, and lead to subsequent
187 degradation of CPEB (Mendez et al., 2000; Thom et al., 2003; Keady et al., 2007; Lapasset et al.,
188 2008; Ochi et al., 2016). The potential Aurora site is conserved in starfish, but we could not detect
189 phosphorylation of this site. Instead, we detected the largest change on Ser32, a site not well
190 conserved, but located near the Thr22 site, a target of Mos-MAPK in *Xenopus* oocytes (Keady et al.,
191 2007). We detected additional CPEB phosphopeptides consistent with hyper-phosphorylation by
192 Cdk1 and Mos-MAPK. The proteomics time course experiment also confirmed that while CPEB is
193 still detectable at MII, levels gradually decrease both in control and U0126-treated samples (Fig.
194 2G). Interestingly, CPEB levels at MI appear somewhat lower in U0126-treated samples as
195 compared to controls that could explain, at least in part, the lower level of Cyclin B in this condition.

196 We detected dephosphorylation of the eIF4E transporter, eIF4ENIF1 a.k.a. 4E-T, which along with
197 CPEB is a core component of the repressive ribonucleoparticle (RNP) keeping mRNAs
198 translationally inactive. We detected peptides of other components of RNPs including eIF4E, DDX6,

199 LSM14 (but not Zar1) (Minshall et al., 2007; Cheng and Schuh, 2024). These proteins are present at
200 constant levels through meiosis, and we saw no significant change in their phosphorylation (Fig. 3B,
201 S2B). We also detected many phosphopeptides of TACC3/Maskin, and while the changes remain
202 below significance, they show a trend towards dephosphorylation (Source Data File 1). This
203 suggests that TACC3/Maskin may play a similar role as in *Xenopus* oocytes and interact with eIF4E
204 to regulate translation (Stebbins-Boaz et al., 1996).

205 Upon CPEB phosphorylation, the repressive complex dissociates and so CPEB can interact with the
206 multi-subunit cleavage and polyadenylation specificity factor (CPSF) to recruit the PolyA
207 polymerase PAP/Gld2 (Mendez et al., 2000; Barnard et al., 2004). Besides Gld2, we observed a
208 change in phosphorylation of several components of the cap-dependent translation initiation
209 complex including the scaffold protein eIF4G that binds to the polyadenylate binding protein
210 PABPC on the semi-circularized mRNA (Wells et al., 1998), and eIF3A involved in the eventual
211 recruitment of the small ribosomal subunit (Aitken and Lorsch, 2012) (Fig. 3B, Table S1).
212 Interestingly, the non-essential initiation factor eIF4B showed increased phosphorylation upon
213 U0126 treatment. While we did not detect a change in phosphorylation, we did detect peptides of
214 most other subunits of the complex, such as the cap binding protein eIF4E, the helicase eIF4A, the
215 polyadenylate binding protein PABPC (Fig. S2B).

216 Interestingly, our top hits also included LARP1, a regulator specific to mRNAs with a 5′ terminal
217 oligopyrimidine (5′TOP), a motif known to associate with mTOR targets (Berman et al., 2021).
218 LARP1 is thought to bind this 5'TOP motif and stabilize the semi-circularized mRNA through
219 interaction with PABPC (Hochstoeger et al., 2024).

220 Another large group of phospho-peptides identified were regulators of the cytoskeleton, a
221 substantial subset of which are involved in centrosomal microtubule nucleation (Fig. 3A, B, Table
222 S1). We found components with roles in centrosome maturation, including proteins involved in the
223 recruitment of the pericentriolar material to centrioles (CEP192, CEP44, and POC1), the main
224 pericentriolar material (PCM) constituent PCM1, as well as the protein furry (FRY)-like, thought to
225 be important for centrosome integrity early in cell division (Ikeda et al., 2012; Conduit et al., 2015).
226 Secondly, we found several proteins that play a role in nucleating and stabilizing astral
227 microtubules including the general microtubule plus tip binding proteins XMAP215/chTOG and
228 CLIP1 (Slep and Vale, 2007), and GTSE1, a plus tip binding protein that specifically regulates the
229 stability of astral microtubules (Bendre et al., 2016). Furthermore, we identified several members
230 of the kinesin superfamily. A kinesin-4 family member (identified as KIF4/21/27) may be involved
231 in separation of spindle poles in anaphase (Bieling et al., 2010), and the kinesin-3 KIF14 may be

required for anaphase in interaction with citron kinase (Gruneberg et al., 2006). Interestingly, a meiosis-specific paralog of KIF14, NabKin was reported to regulate polar body cytokinesis in *Xenopus* oocytes (Samwer et al., 2013).

We also identified several proteins that regulate the actin cytoskeleton (Fig. 3A, B, Table S1). In particular, regulators of the small GTPases Cdc42, Rac1, and RhoA as well as their downstream effectors have been detected. This includes BCR, which is a GTPase-activating protein for Cdc42, as well as the activator of RhoA, MYO9. We detected a significant dephosphorylation of the formin mDia2, which confirms earlier results demonstrating that mDia2 is a downstream target of Mos-MAPK in starfish (Ucar et al., 2013). Additionally, we found a significant effect on the Cdc42 binding protein MRCK, which recently has been shown to drive the initial, meiosis-specific step of polar body cytokinesis (Bourdais et al., 2023). Finally, we found Rac1 that may be involved in Arp2/3-dependent actin nucleation and act as an antagonist of RhoA during polar body cytokinesis, to be dephosphorylated (Halet and Carroll, 2007; Pal et al., 2020).

Taken together, our phosphoproteomic analysis identified well-defined and conserved molecular modules downstream of Mos-MAPK that are involved in the regulation of the meiotic cell cycle, CPE-dependent translation, and the microtubule and actin cytoskeleton. Firstly, these data are consistent with the model proposed in *Xenopus*, whereby Mos-MAPK drives MI-MII transition both by facilitating rapid reactivation of Cdk1 by its dephosphorylation, as well as by triggering translation of Cyclin B and other regulators (Hochegger et al., 2001; Iwabuchi et al., 2000). Our data supports a possible model for translational regulation, by which Mos-MAPK and Cdk1 phosphorylate CPEB leading to the disassembly of repressive RNPs and promote the assembly of the active polyadenylation complex.

Secondly, Mos-MAPK regulates the cytoskeleton to mediate the highly asymmetric oocyte divisions. We identified microtubule regulators including constituents of the centrosome, the pericentriolar material, regulators of microtubule growth at the plus-tips of microtubules, and kinesin motor proteins. These proteins are not part of a single complex, but they do have a common function in organizing centrosomal microtubule arrays. These hits are distinct from regulators of other major pathways of spindle assembly, such as the chromatin-mediated Ran pathway (Valdez et al., 2023). Interestingly, a very recent study found that casein kinase 2 (CK2) specifically regulates the Ran pathway in meiosis (Cantwell et al., 2025). This suggests that there may be multiple kinases regulating different aspects of meiotic spindle assembly with Mos-MAPK specifically acting on astral microtubule arrays.

265 *Mos-MAPK prevents assembly of astral microtubule arrays*

266 To explore the effects of Mos-MAPK on the cytoskeleton in more detail, we recorded the dynamics
267 of MI spindles in 3D at high resolution in live oocytes (Fig. 4A). Quantification of the maximal length
268 of the astral microtubules and the distance between the spindle poles revealed that U0126-treated
269 oocytes display longer astral microtubules and increased pole-to-pole distance. The difference is
270 initially subtle, but it then increases continuously as oocytes progress from prometa- to telophase
271 (Fig. 4A-C). Indeed, Mos-MAPK qualitatively changes the behavior of spindle poles: while in control
272 oocytes with Mos-MAPK active astral microtubules and pole-to-pole distance shortens, in U0126-
273 treated oocytes asters and pole-to-pole distance increases as spindles progress towards telophase
274 (Fig. 4A-C). As a consequence, the first polar body nearly doubles in size and polar body cytokinesis
275 more frequently fails in Mos-MAPK inhibited oocytes (Fig. 4D, E).

276 Next, we performed immunofluorescence stainings to visualize spindle organization at even higher
277 resolution (Fig. 4F). These data corroborated observations made in live oocytes: in normal meiosis
278 centrosomes are almost completely inactive, and chromosomes separate merely by shortening of
279 kinetochore fibers (anaphase A) (Fig. 4F-H). By stark contrast, Mos-MAPK inhibited oocytes display
280 prominent microtubule asters nucleated by centrosomes, which contain numerous and long
281 microtubules (Fig. 4F-H). U0126-treated spindles also display a prominent mid-spindle formed by
282 overlapping microtubules, which drive separation of spindle poles concomitant with shortening of
283 kinetochore fibers in anaphase (anaphase A+B) (Fig. 4F).

284 Taken together, in excellent agreement with the identified phosphoproteins, we show that in
285 unperturbed meiosis I Mos-MAPK activity impedes centrosomal microtubule nucleation, prevents
286 formation of the spindle midzone and anaphase B. If Mos-MAPK is inhibited, the MI spindle adopts a
287 mitotic-like organization with large centrosomal asters and a prominent mid-spindle promoting
288 separation of poles in anaphase B. As a consequence, enlarged polar bodies form and polar body
289 cytokinesis frequently fails. Intriguingly, our data reveal a tight correlation between the maximal
290 length of astral microtubules and pole-to-pole distance, suggesting that the two processes may be
291 functionally linked (Fig. 4B, C, see schematics on Fig. 5E). The explanation for this can be that
292 centrosomal microtubules grow in all directions: away from the spindle as astral microtubules, and
293 into the spindle to form interpolar microtubules. Interpolar microtubules are critical to form the
294 overlapping microtubule bundles at the spindle midzone, pushed apart in anaphase B by PRC1 and
295 kinesin-4 (Bieling et al., 2010). In meiosis, with Mos-MAPK active, both astral and interpolar
296 microtubules are absent, and thus anaphase B does not occur. Through these mechanisms Mos-

297 MAPK functions to minimize polar body size in two ways: by reducing aster size it allows the
298 spindle to localize tightly to the cortex, and by preventing anaphase B it limits the distance between
299 the cortex and the spindle midzone (Fig. 5E). Therefore, Mos-MAPK essentially switches off two
300 mitotic spindle functions: positioning by astral microtubules, and anaphase B that in mitosis is
301 required to move chromosome masses away from the cleavage furrow.

302 In starfish oocytes, unlike in most other species, centrioles are still present at MI (Sluder et al.,
303 1993; Borrego-Pinto et al., 2016a). This might have made the phenotypes easier to interpret than in
304 other species with acentrosomal meiotic spindles. However, acentrosomal microtubule organizing
305 centers (aMTOCs) contain most if not all of the proteins we identified, and functionally replace
306 centriolar centrosomes in oocytes (Mogessie et al., 2018; Schuh and Ellenberg, 2007). Indeed, Mos-
307 MAPK inhibition results in enlarged microtubule asters nucleated from aMTOCs in *Xenopus*, mouse,
308 and *Clytia* oocytes (Verlhac et al., 1996; Bodart et al., 2002; Amiel et al., 2009), and in mouse spindle
309 elongation, i.e. anaphase B was observed in Mos-/- oocytes, very similar to our observations above
310 (Verlhac et al., 2000). This suggests that Mos-MAPK likely has a conserved role in species both with
311 centrosomal and acentrosomal MTOCs. In turn, this meiosis-specific spindle architecture may
312 explain why oocytes employ specialized, actin-driven mechanisms for spindle positioning (Field
313 and Lénárt, 2011).

314

315 *Translation is required to drive meiosis II, but it does not affect spindle architecture*

316 While the observed effects on spindle organization could be fully explained by direct
317 phosphorylation of proteins of the 'microtubule module' we identified, alternatively Mos-MAPK-
318 dependent translation of specific microtubule regulators may also affect spindle architecture. To
319 separate out these effects, we inhibited translation by emetine (Swartz et al., 2021). Emetine-
320 treated oocytes progressed to MI without delay, assembled the MI spindle with apparently normal
321 morphology, and extruded a polar body. Thereafter, a pronucleus formed and oocytes remained in a
322 sustained interphase arrest (Fig. 5A). This confirms that in starfish oocytes new protein synthesis is
323 not needed until the end of MI, however, new protein synthesis is required for progression to MII
324 (Swartz et al., 2021).

325 Next, to investigate effects of translation inhibition on spindle organization, we fixed and stained
326 oocytes at metaphase of MI that were treated with emetine and with emetine and U0126 (Fig. 5B).
327 Emetine alone had no visible effect on spindle organization, whereas a combined treatment with
328 emetine and U0126 resulted in the same phenotype with enlarged asters and pole-to-pole distance

329 as U0126 alone (compare Figs. 4F, G and 5B-D). To specifically test whether translation of Cyclin B -
330 - the protein the levels of which change to the largest extent during meiosis -- has an effect on MI
331 spindle organization, we injected oocytes with a morpholino targeting Cyclin B. While the Cyclin B
332 morpholino caused an effect very similar to translation inhibition by emetine in preventing MII, it
333 had no apparent effect on the morphology of the MI spindle (Fig. S3).

334 Thus, these data together show that in starfish oocytes protein synthesis is not required for meiotic
335 maturation and meiotic progression until the end of MI, however translation of Cyclin B and likely
336 other proteins in required to drive MII. Furthermore, our data show that Mos-MAPK acts on spindle
337 organization independently of its effect on translational regulation.

338

339 *Conclusions*

340 Mos-MAPK and its functions in oocyte meiosis have been studied extensively in the past. These
341 studies evidence that Mos is an 'early invention' already present in the non-bilaterian cnidarian
342 jellyfish, and is thus an ancestral and conserved regulator of oocyte meiosis in metazoa (Amiel et al.,
343 2009). However, likely due to the inherent diversity in cellular morphology and timing of oocyte
344 meiosis among animal species, it remained difficult to identify conserved molecular mechanisms
345 under the control of Mos-MAPK (Dupré et al., 2010). Here, by combining cellular assays with
346 phosphoproteomics we identified the molecular modules controlled by Mos-MAPK; translational
347 regulation by CPE-mediated mRNA polyadenylation, and regulation of astral microtubule arrays.
348 We show how these two processes are critical for switching between mitotic and meiotic division
349 programs, for adapting the cell division machinery to produce the haploid egg ready to be fertilized.

Materials and Methods

Oocyte collection, drug treatments and microinjection

Bat stars (*Patiria miniata*) were obtained in the springtime from Southern California (South Coast Bio-Marine LLC, Monterey Abalone Company, or Marinus Scientific Inc). They were kept at 16˚C for the rest of the year in seawater aquariums at MPI-NAT's Animal Facility. Ovaries and testes were isolated as described previously (Borrego-Pinto et al., 2016). Oocytes were isolated and used immediately or stored for 1-2 days in seawater at 14˚C, for some experiments ovaries were stored for 2-3 days in seawater at 14 ˚C and oocytes were isolated thereafter (Wessel et al., 2010). For fertilization, freshly isolated sperm was added just prior to the emission of the first polar body.

mRNAs and other fluorescent markers were injected using Kiehart chambers and horizontally mounted needles as described previously (Borrego-Pinto et al., 2016; Jaffe and Terasaki, 2004), with the modification that instead of mercury-filled needles, simple back-loaded capillaries were used on a FemtoJet (Eppendorf) injector. mRNA was injected the day before to allow protein expression, whereas fluorescently labeled proteins were injected a few hours prior to imaging.

Meiosis was induced by the addition of 1-methyladenine (1-MA, Acros Organics) at 10 µM final concentration. NEBD started typically 20-25 min after 1-MA addition. U0126 (Sigma) was added simultaneously with 1-MA at 20 µM final concentration. Emetine (Sigma) was added at 10 µM final concentration 30 min before 1-MA.

Every experiment was repeated at least three times, with oocytes taken from at least two different animals.

Fluorescent markers

Chromosomes were labeled by either injecting mRNA encoding human H2B-mCherry or H1 protein purified from calf thymus (Sigma) labeled with AlexaFluor 568 or 647 as described previously (Bun et al., 2018). Microtubules were labeled either by injection of HiLyte488- or HiLyte647-tubulin purified from porcine brain (Cytoskeleton), or recombinant human EB3-mClover protein (gift from So Chun, MPI-NAT). Anti-cyclin B morpholino (TAACCAATGCGAGTTCCGAGGAG, Gene Tools), was injected at 500 µM final concentration immediately before 1-MA stimulation (Swartz et al., 2021).

379 Capped mRNAs with poly-A tail were synthesized from linearized pGEMHE plasmids using the
380 HiScribe™ T7 ARCA mRNA Kit (NEB). The mRNA was purified by Monarch RNA Cleanup Kit (NEB).

381 Active Cdk1-Cyclin B complex was a gift from Pim J. Huis in't Veld and Andrea Musacchio (MPI for
382 Molecular Physiology, Dortmund, Germany) (Huis In 't Veld et al., 2022). In order to remove
383 glycerol, the complex was purified through a 10K MWCO protein concentrator (Pierce) and
384 dissolved in PBS with 200 mM sucrose. The activity of the complex was confirmed by its ability to
385 cause maturation in starfish oocytes. The Cdk1-Cyclin B complex was injected into the U0126-
386 treated oocytes directly after the first polar body extrusion.

387

388 *Live cell microscopy*

389 Starfish oocytes were imaged directly in the injection chambers. Live-cell images were acquired
390 either on a Visitron Systems (Puchheim, Germany) spinning disk confocal microscope or on a Zeiss
391 LSM780 (Jena, Germany) laser scanning confocal microscope. The spinning disk system is based on
392 a Nikon Ti2 microscope body equipped with a Yokogawa W1 scanhead and two Prime BSI cameras
393 (Teledyne Photometrics). On the laser scanning microscope, we used a C-Apochromat 40x 1.20 NA
394 objective lens with the following settings: imaging area 100 µm×100 µm, pixel size 200 nm, 15 z-
395 slices with 2 µm step size, pinhole set to 2 AU, time intervals 3-5 min. On the spinning disk
396 microscope, we used a CFI SR Plan Apo IR 60x 1.27 NA water immersion objective. Typical settings
397 were: exposure time 200 ms, pixel size 110 nm, 11-15 z-slices with 3 or 4 µm step size, time
398 intervals 3-5 min. Images of the control and experimental groups were acquired under identical
399 imaging conditions on the same microscope. All live imaging experiments were carried out at 20°C.

400

401 *Immunostaining*

402 Oocytes were fixed at the desired times in a PFA/GA fixative (100 mM HEPES [pH 7.0], 50 mM
403 EGTA, 10 mM $MgSO_4$, 0.5% Triton-X100, 400 mM sucrose, 2% formaldehyde, and in some
404 experiments 0.2% glutaraldehyde) modified from (Strickland et al., 2004). Subsequently, samples
405 were permeabilized and blocked in blocking buffer (PBS + 0.1% Triton-X100 plus 3% BSA and the
406 Image-IT reagent (Thermo Scientific)). Antibody staining was done for 24 h in a blocking buffer at
407 room temperature with the primary antibody premixed with secondary nanobodies/Fab fragment.
408 Microtubules were labeled with anti-α-tubulin mouse antibody (DM1A, Sigma), and lamin was

409 labeled with a custom-made rabbit polyclonal antibody (Wesolowska et al., 2020) primarily labeled
410 with Alexa 488 NHS ester (Thermo Scientific) according to the manufacturer's instructions.
411 Secondary staining was done by anti-mouse secondary nanobodies with Atto-488 (NanoTag,
412 #N2002-At488-S) or donkey Fab anti-mouse IgG AlexaFluor594 (Jackson, #715-587-003). DNA was
413 labeled with Hoechst 33342 (Thermo Scientific). Oocytes were mounted in PBS or in the antifade
414 agent ProLong Glass or SlowFade Diamond (Thermo Scientific). Fixed oocytes were imaged on the
415 same microscope systems as used for live imaging with the following modifications: for the
416 spinning disk confocal microscope, exposure time of 200 ms, pixel size of 110 nm, and 70 z-slices
417 with 200 or 600 nm step size. On the laser scanning system, we used a pixel size of 40 nm, 80 z-
418 slices with 200 nm step size, pinhole set to 1 Airy unit.

419

420 *Image analysis*

421 Prior morphometric quantification, immunofluorescent images were deconvolved using the
422 Huygens software (Scientific Volume Imaging) with either confocal, AiryScan, or spinning disk
423 settings as appropriate. Quantification was done in ImageJ/FIJI (Schindelin et al., 2012). Images
424 were rotated and resliced in XY and XZ planes to orient the spindle orthogonally. The quantification
425 of spindle length and diameter of centrosomes were done by measuring the half-maximal width of
426 the intensity profile along the respective structures along the spindle axis. Statistical analysis was
427 performed by Excel (Microsoft), results were plotted in R (R Core Team).

428 The maximal length of microtubules and spindle diameter were quantified on live images using
429 ImageJ/FIJI (Schindelin et al., 2012) in a maximal Z-projected volume slab of 10 µm thickness. The
430 maximal length of microtubules was estimated by measuring the distance of aster tips to the
431 centriole (live labeled by EB3-mClover or by anti-tubulin-staining in fixed samples) and the pole
432 distance was measured by placing points at each pole and calculating their 3D distance. Statistical
433 analysis was performed by using Excel (Microsoft), results were plotted in R (R Core Team).

434 For presenting images on figures, we typically used a Gaussian blur of 0.5-1 pixels to reduce shot
435 noise. Images were adjusted for brightness and contrast, and where indicated, gamma adjustments
436 were applied.

437

438 *Western Blots*

439 Approximately 50 oocytes were collected for each condition at the stated time points, lysed in SDS
440 sample loading buffer (62.5 mM TRIS, pH 6.8, 1.5% SDS, 0.5 M sucrose, 25 mM DTT, 0.002%
441 bromophenol blue) and heated at 95°C for 10 minutes. Proteins were resolved using SDS-PAGE
442 performed on 4-12% Bis-Tris gels (Thermo) and transferred to a nitrocellulose membrane
443 (Thermo, #88025) for Western blotting. Anti phospho-p44/42 MAPK (Erk1/2) antibody (Cell
444 Signaling Technology, #9101) was diluted to 1:3000, anti phospho-cdc2(Tyr15) antibody (Cell
445 Signaling Technology, #9111) to 1:1000 and anti-alpha tubulin (DM1A) to 1:1000 in 5% BSA made
446 in TBST (TBS with 0.1% Tween-20). Fluorescently labeled anti-mouse CF770 (Biotium,
447 #20077)/anti-mouse CF680 (Biotium, #20065) and anti-rabbit CF680 (Biotium, #20418)/anti-
448 rabbit CF770 (Biotium, #20484) secondary antibodies were diluted to 1:10000 in TBST before use.
449 All immunoblots were scanned on a LI-COR Odyssey imager.

450

451 *Sample preparation and LC/MS analysis*

452 Two or three biological replicates of oocytes were collected from different starfish animals for the
453 proteomics and phosphoproteomics experiments, respectively (see schematics on Fig 2A and E).
454 Oocytes were matured by addition of 1-MA and were simultaneously treated with 20 µM U0126 or
455 equal amount of DMSO. Maturation timing was tested in prior experiments and was also directly
456 monitored under a dissecting microscope. Synchronicity of oocytes was confirmed by staining a
457 small portion of the collected oocytes with Hoechst 33342 and imaging on a confocal microscope.
458 We confirmed a synchronicity of 92-96% of all samples analyzed.

459 For the phosphoproteomics experiment, 20 µl of starfish oocytes were lysed on ice in SDS lysis
460 buffer (4% [w/v] SDS, 150 mM Hepes-KOH pH 7.0, 2 mM dithiothreitol (DTT), 10 mM EDTA, 250
461 mM sucrose, and protease inhibitor cocktail [Complete Roche Mini]). The mechanical cell
462 disruption was done by centrifuging oocytes through a 40 µm mesh at 7000 g. Samples were
463 diluted to a final 0.1% SDS and 1 mM $MgCl_2$ was added. Proteins were reduced with 5 mM DTT for
464 30 min at 37°C, 300 rpm, and alkylated with 10 mM iodoacetamide (IAA) for 30 min at 25°C, 300
465 rpm, in the dark. The reaction was quenched with 10 mM DTT for 5 min at 25°C, 300 rpm.

466 Sample cleanup was performed by applying a single-pot, solid-phase-enhanced sample preparation
467 protocol (Hughes et al., 2019). Briefly, carboxylate-modified magnetic beads (Cytiva
468 65152105050350, 45152105050250, mixed 1:1) were added at a 1:10 protein-to-bead mass ratio
469 with an equal volume of 100% [v/v] acetonitrile (ACN). Beads were washed twice with 80% [v/v]

470 EtOH and once with 100% [v/v] ACN. Proteins were digested in 50 mM TEAB containing trypsin
471 (Promega) at a 1:20 enzyme-to-protein ratio overnight at 37 °C, 1000 rpm. Peptides were removed
472 from the magnetic beads and aliquots were taken for whole proteome analysis.

473 Residual samples were subjected to phosphopeptide enrichment according to the EasyPhos
474 protocol (Humphrey et al., 2015). Briefly, peptide mixtures were adjusted to final 228 mM KCl, 3.9
475 mM KH_2PO_4, 38% [v/v] ACN, 4.5% [v/v] trifluoroacetic acid (TFA), mixed and cleared by
476 centrifugation. TiO_2 beads (10 µm, GL Sciences) in 80% ACN, 6% TFA were added at a beads-to-
477 protein ratio of 10:1. Peptides were incubated with beads for 20 min at 40°C, 1000 rpm. Beads were
478 resuspended and washed in 60% [v/v] ACN, 1% [v/v] TFA four times. Finally, beads were
479 resuspended in 80% [v/v] ACN, 0.5% [v/v] acetic acid and transferred to empty columns (Harvard
480 Apparatus, 74□3840). Phosphopeptides were eluted in two steps with 40% [v/v] ACN, 15% [v/v]
481 NH_4OH.

482 TMTsixplex™ (Thermo Scientific) labeling was performed according to manufacturer's instructions.
483 Whole proteome and phosphopeptide-enriched samples were labeled separately. Both were further
484 cleaned using C18 MicroSpin columns (Harvard Apparatus) according to manufacturer's
485 instructions. Samples were dissolved in 10 mM NH_4OH pH 10, 5% [v/v] ACN and peptides were
486 loaded onto an Xbridge C18 column (Waters) using an Agilent 1100 series chromatography system.
487 The column was operated at a flow rate of 60 µl/min with a buffer system of buffer A, 10 mM
488 NH_4OH pH 10; and buffer B, 10 mM NH_4OH pH10, 80% [v/v] ACN. The column was equilibrated
489 with 5% B and separation was performed over 64 min using the following gradient: 5% B (0-7
490 min), 8-30% B (8-42 min), 30-50% B (43-50 min), 90-95% B (51-56 min), 5% B (57-64 min). For
491 phosphopeptides, the first 6 min were collected as flow-through (FT), followed by 48x1 min
492 fractions, which were reduced to 23 fractions by concatenated pooling. The remaining fractions
493 were discarded. For the whole proteome sample, 54x1 min fractions were collected and combined
494 to 19 final fractions. The remaining fractions were discarded. Fractionated whole proteome and
495 phosphopeptide samples were dried in a speed vac concentrator and subjected to LC-MS/MS
496 analysis.

497 For the proteomics time course experiment, oocytes were collected, pelleted and lysed in SDS lysis
498 buffer (4% [w/v] SDS, 150 mM Hepes-NaOH pH 7.5, 1x Roche Protease inhibitor cocktail) by
499 incubation for 5 min, 99°C; by sonication, in alternating 30 s on- and 30 s off-cycles at highest
500 intensity output (Bioruptor, Diagenode); and by another incubation for 5 min, 99°C. Protein
501 concentrations were determined using Pierce™ BCA Protein Assay Kit - Reducing Agent Compatible

502 (Thermo Scientific; 23250). Proteins were reduced with 10 mM dithiothreitol (DTT) for 30 min at
503 37°C, 300 rpm, and alkylated with 40 mM iodoacetamide (IAA) for 30 min at 25°C, 300 rpm, in the
504 dark. The reaction was quenched with 10 mM DTT for 5 min at 25°C, 300 rpm. Aliquots containing
505 0.1 mg of protein for each replicate of each sample were further processed. Samples were diluted to
506 final 0.4% [w/v] SDS and 1 mM $MgCl_2$ was added. DNA content was digested using 312.5 U of
507 Pierce™ Universal Nuclease (Thermo Scientific) for 2 hrs at 37°C, 300 rpm. Samples were cleaned
508 up by single-pot, solid-phase-enhanced sample preparation protocol as above. Peptides were
509 recovered from the magnetic beads and beads were washed once with 100 uL water. Samples were
510 dried in a speed vac. Samples were measured using DIA.

511

512 *Proteomics data analysis*

513 The proteome database was compiled using datasets at Echinobase v2 (echinobase.org) (Kudtarkar
514 and Cameron, 2017) and NCBI annotation (RefSeq ID 23626818) for *Patiria miniata*. The available
515 protein sequences were clustered with mmseqs2 easy-clust workflow (Steinegger and Söding,
516 2018) with a sequence similarity threshold of 0.95 to obtain a non-redundant set of representative
517 sequences. Transcript sequences for Echinobase v2 were derived from the genome sequence and
518 transcriptome annotation with gffread tool (Pertea and Pertea, 2020). The representative
519 transcripts were annotated via TRAPID web interface (Bucchini et al., 2021) using EggNOG 4.5.1
520 database (Huerta-Cepas et al., 2016). Full log of TRAPID annotation is deposited at
521 https://doi.org/10.25625/03K7BQ. In addition, manually curated protein sequences for selected
522 proteins of interest were included into the proteome. TRAPID gene identifiers and ontology terms
523 were used for the downstream over-representation analysis.

524 Raw phospho-TMT mass spectrometry data were processed using MaxQuant version 1.6.17.0 (Cox
525 and Mann, 2008). MaxQuant output tables were filtered to remove decoys, contaminants and low-
526 confidence peptides with posterior error probability (PEP) >= 0.01. Ratios of phospho-peptide
527 intensities to the corrected parent protein intensities were log2-transformed and used for
528 subsequent differential expression analysis. The protein groups were not post-filtered by identified
529 unique peptides or q-values to maximize the match with phospho-peptides, resulting in 76% of
530 phospho-peptides having a corresponding total protein intensity for normalization.

531 A linear model testing for the difference between means of phospho-peptide ratios in treatment
532 and control groups was fit with least-squares, and p-values were estimated with the empirical
533 Bayes approach via *limma* R package (Ritchie et al., 2015). Multiple hypothesis correction was done

using the Benjamini and Hochberg approach for false discovery rate (FDR) estimation and a threshold of p-adjusted <=0.05 was set (Benjamini and Hochberg, 1995).

Gene ontology over-representation analysis was performed using the *g:Profiler* tool g:GOSt using the default p-value adjustment strategy "g_SCS" and a significance threshold of 0.05 (annotation available with identifier "gp__EGla_34PO_4UY") (Raudvere et al., 2019).

The heatmap of all significantly differentially phosphorylated sites was made from the normalized ratios of significantly up- and down- regulated phosphopeptides scaled to the mean of 0 and standard deviation of 1. Plotting was done via the *pheatmap* R package with "ward.D2" clustering method (Murtagh and Legendre, 2014) and euclidean distance as a metric (Kolde, 2025).

The Phospho (STY) probabilities for each tested peptide sequence were mean-aggregated on amino acid level across all peptide-spectrum matches (PSMs) and the most likely amino acid per peptide sequence was treated as phosphorylated. Peptide sequences, log2-fold changes and p-values of differential expression were submitted for kinase prediction at phosphosite.org(Hornbeck et al., 2015). Top significantly downregulated kinases that passed the p-adjusted threshold of 0.05 were reported. Phosphosite motifs were derived by centering all the differentially dephosphorylated peptides (q-value < 0.05) around the most likely phospho-sites as a foreground, compared to the background of all dephosphorylated peptides and plotted via *Logolas* R package (Dey et al., 2018). Kinase-specific motifs were derived from a set of significantly de-phosphorylated peptides having the kinase of interest in the top-10 predicted targets.

Data-independent acquisition (DIA) proteomics was processed with DIA-NN using the default settings (Demichev et al., 2020), and the signal intensity was post-aggregated with the MaxLFQ algorithm upon the following PSM-level filters: Q-value <= 0.001 and Protein Group Q-value <= 0.05. Same as for phospho-TMT, the differential expression was assessed via "limma", with additional weights of 0.05 assigned to the missing values, conservatively imputed by minimal replicate intensity. The thresholds of adjusted p-value (BH procedure) of 0.05 and a log2FoldChange of 0.5 were chosen to define reliably quantified proteins with a large enough effect size.

Statistical analyses

Statistical comparisons were done using the Mann-Whitney test or a two-tailed T-test, as indicated in the figure legend. ** denotes p<0.05, and *** denotes p<0.0001. Data distribution was assumed to be normal but this was not formally tested. Computational and statistical analysis has been

implemented in R v4.1.1 (Ihaka and Gentleman, 1996) or in Excel (Microsoft) and subsequently plotted in R.

Online supplemental material

This manuscript contains 4 Supplementary Figures/Tables and 4 Source Data Files. Fig. S1 shows experiments to determine the effective dose of U0126, and morphometric analyses of spindles treated with U0126; Fig. S2 shows further analyses of the proteomics experiments; Table S1 shows tabulated data for the functional modules shown on Fig. 3B; Fig S3 shows the effect of preventing Cyclin B synthesis during meiosis. The Source Data Files include the complete phosphoproteomics dataset (Source Data File 1), the complete proteomics time course dataset (Source Data File 2), the significant hits of the phosphoproteomics experiment (Source Data File 3), and the uncropped membranes of the Western blots shown (Source Data File 4 and 5).

Data and availability

No new or unique reagents were generated in this study.

The TRAPID protein database used for searching the proteomics data is available at GRO.data at https://doi.org/10.25625/03K7BQ . The mass spectrometry proteomics datasets for starfish oocytes are available in PRIDE (Perez-Riverol et al., 2022) and UCSD MassIVE member repositories of the ProteomeXchange Consortium with the project accession identifiers PXD043650 and PXD067579 | MSV000098905, respectively.

Acknowledgements

We thank all members of the Lenart laboratory at MPI-NAT for protocols, reagents and support, in particular Jasmin Jakobi and Antonio Politi. We thank MPI-NAT's Animal Facility, specifically Sascha Krause and Ulrike Teichmann. We would like to thank So (Nick) Chun and Melina Schuh for providing the recombinant EB3-mClover3 protein, Pim J Huis In't Veld and Andrea Musacchio for Cdk1-Cyclin B complex and Dirk Görlich for Gibson assembly kit. I.A. is a member and has been partially funded by the IMPRS Molecular Biology Programme. The laboratory of P. L. is funded by the Max Planck Society, H. U. receives additional funding by the Deutsche Forschungsgemeinschaft

(DFG) through SFB1565 (project number 469281184), Collaborative Research Centre SFB1565. The authors declare no competing financial interests.

Author contributions

I.A. and P.L. designed and conceptualized the experiments. I.A, P.M., M.C., A.O. conducted experiments and analyzed data. L.W. under the supervision of H.U. carried out the phosphorproteomics analysis. Y.H. under the supervision of J.L. analyzed the proteomics data and carried out other bioinformatics analyses. P.L. analyzed data and wrote the manuscript. I.A, P.M. and Y.H. revised and improved the manuscript.

606 **Figure legends**

607

608 **Figure 1. Mos-MAPK inhibition prevents MII leading to parthenogenetic development**

609 **(A)** Western blot of a time course using phospho-MAPK (marking activated MAPK) and phospho-
610 Cdk1 (marking the inactive Tyr15 phosphorylated form) antibodies to monitor Mos-MAPK and
611 Cdk1 activities during meiosis of starfish oocytes. Oocytes were treated with 20 µM U0126 or equal
612 amount of DMSO added simultaneously with the maturation hormone. Timepoints are indicated as
613 minutes after NEBD. Fertilization was performed 60 minutes after NEBD. Numbers to the left are in
614 kDa and mark the position of the molecular weight markers. For the complete blots see Source Data
615 File 4.

616 **(B)** Selected frames from time-lapse recording of oocytes expressing H2B-mCherry (red) and
617 injected with HiLyte488-tubulin (cyan) to label chromosomes and microtubules, respectively.
618 Oocytes were imaged through meiosis and then fertilized after meiosis I while imaging on a
619 spinning disk confocal microscope. Before inducing maturation, oocytes were treated either with
620 20 µM U0126 or an equal amount of DMSO. PBI and outlines indicate the polar bodies. Venus and
621 Mars signs indicate female and male pronuclei respectively. Insets show magnified views of
622 chromosomes. Maximum intensity projections are shown, scale bars are 20 µm (insets 5 µm), and
623 time is given in minutes.

624 **(C)** Individual data points and boxplot showing the time from nuclear envelope breakdown (NEBD)
625 to metaphase I quantified on recordings similar to shown in (B). Statistical comparison was done
626 using the Mann-Whitney test, n marks the number of oocytes imaged.

627 **(D)** Individual data points and boxplot showing the time from meiotic metaphase I to the first
628 mitotic metaphase quantified on recordings similar to those shown in (B). Statistical comparison
629 was done using the Mann-Whitney test, n marks the number of oocytes imaged.

630 **(E)** Immunofluorescence images of oocytes stained for microtubules (anti-tubulin, cyan), chromatin
631 (Hoechst 33342, red), and the lamina (anti-lamin B, green). Oocytes were treated with 20 µM
632 U0126 or an equal amount of DMSO and then fixed 60 and 120 minutes after NEBD, respectively.
633 Samples were imaged on a spinning disk microscope. Maximum intensity projections are shown,
634 scale bars are 10 µm.

(F) Selected frames from a time-lapse recording of oocytes expressing H2B-mCherry (red) and injected with HiLyte488-tubulin (cyan) to label chromosomes and microtubules, respectively. Oocytes were imaged through meiosis on a spinning disk confocal microscope. Before inducing maturation, oocytes were treated with 20 μM U0126. Then oocytes were either left unmanipulated or they were injected with active Cdk1-Cyclin B protein immediately following extrusion of the first polar body. Maximum intensity projections are shown, scale bars are 20 μm, and time is given in minutes. PB I denotes the first polar body, and PN is the pronucleus.

Figure 2. Overview of the proteomics and phosphoproteomics experiments

(A) Outline of the phosphoproteomics experiment. Mos-MAPK-inhibited (20 μM U0126, purple) and control (DMSO, green) oocytes were collected at metaphase I in three biological replicates and processed for phosphoproteomics. For the complete dataset see Source Data File 1.

(B) Unsupervised clustering of differentially phosphorylated peptides (rows) vs TMT channels (columns). Green: control, purple: Mos-MAPK inhibition. TMT reporter intensity values are scaled to mean of 0 and SD of 1.

(C) Gene ontology (GO) over-representation analysis of differentially phosphorylated proteins. The numbers indicate the gene set sizes and a number of differentially phosphorylated proteins.

(D) Prediction of human effector kinase families from the differentially de-phosphorylated sites.

(E) Outline of the proteomics time course experiment. Mos-MAPK-inhibited (20 μM U0126, purple) and control (DMSO, green) oocytes were collected at the specified stages at the given times in two biological replicates. Samples were processed in 3 technical replicates for proteomics and analyzed by DIA. For the complete dataset see Source Data File 2.

(F) Unsupervised clustering of centered DIA intensities of 2 biological and 3 technical replicates (columns). Green: control, purple: Mos-MAPK inhibition.

(G) Log10 normalized protein intensities for the indicated proteins. Mean and standard error of the two biological replicates and three technical repetitions of each are shown.

Figure 3. Phosphoproteomics reveals cell cycle, cytoskeleton and translation as the main processes regulated by Mos-MAPK

664 **(A)** Volcano plot of the quantified phosphopeptides. The majority of phosphopeptides were
665 manually classified into four categories: Translation, Cytoskeleton, Cell cycle regulation, and MAPK
666 pathway. The rest of the phosphopeptides including those from unidentified proteins are marked as
667 gray dots. For the complete dataset see Source Data Files 1 and 3.

668 **(B)** Functional modules were manually assembled from the list of significantly affected
669 phosphopeptides. Color code indicates the average Log2 fold change in phosphopeptide abundance
670 upon Mos-MAPK inhibition. The numerical data is shown in a tabulated form on Table S1.

671

672 **Figure 4. Mos-MAPK reduces aster growth to minimize polar body size**

673 **(A)** Selected frames from a time-lapse recording of the microtubule spindle in an oocyte undergoing
674 meiosis I on a spinning disk confocal microscope. Chromosomes are labeled with H1-Alexa568
675 (red) and microtubule plus tips by EB3-mClover3 protein (cyan). Before inducing maturation, the
676 oocyte was treated with either 20 μM U0126 or an equal amount of DMSO. (left) overlay of the two
677 fluorescent channels; (middle) the EB3-mClover3 channel is shown with adjusted gamma; (right)
678 3D rendering of the centrosome (cyan) and chromosomes (red). Maximum intensity projections are
679 shown, scale bars are 20 μm.

680 **(B, C)** 3D distances of the spindle poles and the maximal length of astral microtubules at different
681 stages of meiosis I are quantified on recordings similar to (A). n refers to the number of individual
682 oocytes analyzed.

683 **(D)** Boxplot showing quantification of polar body sizes on transmitted light microscopy images. n
684 refers to the number of individual oocytes analyzed. ***$p<0.0001$, statistical comparison was done
685 using a two-tailed T-test.

686 **(E)** Bar chart showing the success rate of polar body formation. Polar bodies were counted by live
687 imaging in H1-Alexa568-injected oocytes after completion of meiosis. n refers to the number of
688 individual oocytes analyzed.

689 **(F)** Immunofluorescence images of oocytes stained for microtubules (anti-tubulin, cyan), and
690 chromatin (Hoechst 33342, red). Oocytes were treated with 20 μM U0126 or an equal amount of
691 DMSO, and then fixed at the stages indicated. Imaging was done using spinning disk confocal
692 microscopy. Maximum intensity projections are shown, scale bar is 20 μm. Lower panels show the
693 tubulin channel separately and with adjusted gamma (0.5).

694 **(G)** Quantification of the 3D distance between spindle poles on data similar to shown in (F).
695 **p<0.05, ***p<0.0001 in two-tailed T-tests.

696 **(H)** Single optical sections crossing the centrosomes selected from the projected images shown in
697 (F). Images are shown after gamma adjustment (0.5), scale bar is 10 µm.

698

699 **Figure 5. Translation is required for MII transition, but it does not affect spindle morphology**

700 **(A)** Selected frames from a time-lapse recording of an oocyte injected with H1-Alexa647 (red) and
701 HiLyte488-tubulin (cyan) to label chromosomes and microtubules, respectively. The oocyte was
702 imaged through meiosis on a spinning disk confocal microscope. Before inducing maturation, the
703 oocyte was treated with 10 µM emetine to block translation. Maximum intensity projections are
704 shown, the scale bar is 20 µm, and time is given in minutes. PB I denotes the first polar body, and
705 PN is the pronucleus.

706 **(B)** Oocytes fixed at metaphase I and stained for microtubules (anti-tubulin, cyan), chromatin
707 (Hoechst 33342, red). Oocytes were treated with emetine and DMSO or 20 µM U0126. 3D stacks
708 were acquired on a spinning disk microscope. Maximum intensity projections are shown, scale bars
709 are 20 µm.

710 **(C, D)** Boxplots showing a comparison of the pole-to-pole distance and maximal length of
711 microtubules at metaphase I between emetine and emetine+U0126 treated oocytes as shown on
712 (B). Statistical comparison was done using a two-tailed T-test.

713 **(E)** Mos-MAPK specifically downregulates pericentriolar material proteins, reduces the growth and
714 number of astral and interpolar microtubules, and prevents Anaphase B, thereby minimizing the
715 size of the polar body. Bottom: schematic illustration of correlated changes in aster size and pole
716 distance. Mean values shown on Fig. 4B and C are plotted on a schematic of the spindle.

717

718

719 **Supplemental Figure Legends**

720

721 **Figure S1. U0126 effectively and specifically inactivates Mos-MAPK in starfish oocytes and**
722 **alters spindle morphology**

723 **(A)** Oocytes were treated with the indicated concentrations of U0126 concomitant with maturation
724 hormone addition. Thereafter maturation was monitored by videomicroscopy, of which selected
725 frames are shown at the start of the recording and 60 minutes after hormone addition.

726 **(B)** Western blots of oocytes treated as in (A) using phospho-MAPK and phospho-Cdk1 antibodies
727 to monitor Mos-MAPK and Cdk1 activities, respectively. Numbers to the left are in kDa and mark
728 the position of the molecular weight markers. For the complete blots see Source Data File 4.

729 **(C)** Immunofluorescence images of oocytes stained for microtubules (anti-tubulin, cyan) and
730 chromatin (Hoechst 33342, red) at the indicated stages and treated with 20 µM U0126 or an equal
731 amount of DMSO. Imaging was done on a laser scanning confocal microscope. Maximum intensity
732 projections are shown, scale bars are 20 µm.

733 **(D)** Schematics of the meiotic spindle illustrating the morphometric measurements. Microtubules
734 are cyan, chromatin is red.

735 **(E)** Individual data points and boxplots showing 3D measurements performed on images similar to
736 those shown in (C). **$p<0.05$, ***$p<0.0001$, statistical analysis was done using a two-tailed T-test. n
737 is the number of oocytes analyzed.

738

739 **Figure S2. Further analyses of the proteomics experiments**

740 **(A)** Logo motif representation of the consensus site of all differentially phosphorylated peptides in
741 the phosphoproteomics experiment. Peptides were grouped based on the kinases that would be
742 most likely to be responsible for their phosphorylation. Logo motif representation of the consensus
743 sequence for each group most likely to be phosphorylated by Mos, MAPK, RSK and Cdk1/2,
744 respectively. The y-axis shown the information content that was scaled between 0 and 1 for each of
745 the kinase targets.

(B) Log10 normalized protein intensities for the indicated proteins in the proteomics time course experiment. Mean and standard error are shown of the two biological replicates and three technical repetitions of each.

Figure S3. Preventing Cyclin B synthesis blocks MII transition, but it does not affect MI spindle morphology

(A) Selected frames from a time-lapse recording of oocytes injected with H1-Alexa647 (red) and HiLyte488-tubulin (cyan) to label chromosomes and microtubules, respectively. Oocytes were imaged through meiosis on a spinning disk confocal microscope. Before inducing maturation, oocytes were injected with either a morpholino targeting Cyclin B or water as control. Maximum intensity projections are shown, scale bars are 20 µm, and time is given in minutes. PB I and II denote the first and second polar bodies, respectively; PN is the pronucleus.

(B) Individual data points and boxplots showing a comparison of the maximal length of microtubules at metaphase I between control and Cyclin B morpholino injected oocytes. Statistical comparison was done using a two-tailed T-test, n is the number of oocytes analyzed.

Supplemental Tables

Table S1. Tabulated data for the functional modules shown on Fig. 3B

Manually annotated functional modules are listed, color code indicates the average Log2 fold change in phosphopeptide abundance upon Mos-MAPK inhibition.

Source Data Files

Source Data File 1. The phosphoproteomics dataset (DDA-TMT)

Differential expression analysis (DEA) of the ratios of phosphorylated peptides to their total protein intensities in U0126 versus DMSO treated samples.

Source Data File 2. The proteomics time course experiment (DIA)

775 Differential expression analysis (DEA) of the peptides to their total protein intensities in the
776 different conditions relative to the MI control (DMSO) sample.

777

778 **Source Data File 3. Significant hits of the phosphoproteomics experiment**

779 Results of the manual annotation of the significant hits (p-adj>0.05) from the differential
780 expression analysis (DEA).

781

782 **Source Data Files 4. and 5. Uncropped images of Western blots**

783

References

Abrieu, A., M. Dorée, and D. Fisher. 2001. The interplay between cyclin-B-Cdc2 kinase (MPF) and MAP kinase during maturation of oocytes. *J. Cell Sci.* 114:257–267. doi:10.1242/jcs.114.2.257.

Aitken, C.E., and J.R. Lorsch. 2012. A mechanistic overview of translation initiation in eukaryotes. *Nat. Struct. Mol. Biol.* 19:568–576. doi:10.1038/nsmb.2303.

Amiel, A., L. Leclère, L. Robert, S. Chevalier, and E. Houliston. 2009. Conserved functions for Mos in eumetazoan oocyte maturation revealed by studies in a cnidarian. *Curr. Biol. CB*. 19:305–311. doi:10.1016/j.cub.2008.12.054.

Araki, K., K. Naito, S. Haraguchi, R. Suzuki, M. Yokoyama, M. Inoue, S. Aizawa, Y. Toyoda, and E. Sato. 1996. Meiotic abnormalities of c-mos knockout mouse oocytes: activation after first meiosis or entrance into third meiotic metaphase. *Biol. Reprod.* 55:1315–1324. doi:10.1095/biolreprod55.6.1315.

Arumugam, K., Y. Wang, L.L. Hardy, M.C. MacNicol, and A.M. MacNicol. 2010. Enforcing temporal control of maternal mRNA translation during oocyte cell-cycle progression. *EMBO J.* 29:387–397. doi:10.1038/emboj.2009.337.

Barnard, D.C., K. Ryan, J.L. Manley, and J.D. Richter. 2004. Symplekin and xGLD-2 are required for CPEB-mediated cytoplasmic polyadenylation. *Cell*. 119:641–651. doi:10.1016/j.cell.2004.10.029.

Belloc, E., and R. Méndez. 2008. A deadenylation negative feedback mechanism governs meiotic metaphase arrest. *Nature*. 452:1017–1021. doi:10.1038/nature06809.

Bement, W.M., and D.G. Capco. 1990. Transformation of the amphibian oocyte into the egg: structural and biochemical events. *J. Electron Microsc. Tech.* 16:202–234. doi:10.1002/jemt.1060160303.

Bendre, S., A. Rondelet, C. Hall, N. Schmidt, Y.-C. Lin, G.J. Brouhard, and A.W. Bird. 2016. GTSE1 tunes microtubule stability for chromosome alignment and segregation by inhibiting the microtubule depolymerase MCAK. *J. Cell Biol.* 215:631–647. doi:10.1083/jcb.201606081.

Benjamini, Y., and Y. Hochberg. 1995. Controlling the False Discovery Rate: A Practical and Powerful Approach to Multiple Testing. *J. R. Stat. Soc. Ser. B Methodol.* 57:289–300.

Berman, A.J., C.C. Thoreen, Z. Dedeic, J. Chettle, P.P. Roux, and S.P. Blagden. 2021. Controversies around the function of LARP1. *RNA Biol.* 18:207–217. doi:10.1080/15476286.2020.1733787.

Bhatt, R.R., and J.E. Ferrell. 1999. The protein kinase p90 rsk as an essential mediator of cytostatic factor activity. *Science*. 286:1362–1365. doi:10.1126/science.286.5443.1362.

Bieling, P., I.A. Telley, and T. Surrey. 2010. A Minimal Midzone Protein Module Controls Formation and Length of Antiparallel Microtubule Overlaps. *Cell*. 142:420–432. doi:10.1016/j.cell.2010.06.033.

Bodart, J.-F.L., D.V. Gutierrez, A.R. Nebreda, B.D. Buckner, J.R. Resau, and N.S. Duesbery. 2002. Characterization of MPF and MAPK activities during meiotic maturation of Xenopus tropicalis oocytes. *Dev. Biol.* 245:348–361. doi:10.1006/dbio.2002.0647.

Borrego-Pinto, J., K. Somogyi, M.A. Karreman, J. König, T. Müller-Reichert, M. Bettencourt-Dias, P. Gönczy, Y. Schwab, and P. Lénárt. 2016a. Distinct mechanisms eliminate mother and daughter centrioles in meiosis of starfish oocytes. *J. Cell Biol.* 212:815–827. doi:10.1083/jcb.201510083.

Borrego-Pinto, J., K. Somogyi, and P. Lénárt. 2016b. Live Imaging of Centriole Dynamics by Fluorescently Tagged Proteins in Starfish Oocyte Meiosis. *Methods Mol. Biol. Clifton NJ*. 1457:145–166. doi:10.1007/978-1-4939-3795-0_11.

Bourdais, A., B. Dehapiot, and G. Halet. 2023. MRCK activates mouse oocyte myosin II for spindle rotation and male pronucleus centration. *J. Cell Biol.* 222:e202211029.

doi:10.1083/jcb.202211029.
Bucchini, F., A. Del Cortona, Ł. Kreft, A. Botzki, M. Van Bel, and K. Vandepoele. 2021. TRAPID 2.0: a web application for taxonomic and functional analysis of de novo transcriptomes. *Nucleic Acids Res.* 49:e101. doi:10.1093/nar/gkab565.
Bun, P., S. Dmitrieff, J.M. Belmonte, F.J. Nédélec, and P. Lénárt. 2018. A disassembly-driven mechanism explains F-actin-mediated chromosome transport in starfish oocytes. *eLife*. 7:e31469. doi:10.7554/eLife.31469.
Burdyniuk, M., A. Callegari, M. Mori, F. Nédélec, and P. Lénárt. 2018. F-Actin nucleated on chromosomes coordinates their capture by microtubules in oocyte meiosis. *J. Cell Biol.* 217:2661–2674. doi:10.1083/jcb.201802080.
Cao, L.-R., J.-C. Jiang, and H.-Y. Fan. 2020. Positive Feedback Stimulation of Ccnb1 and Mos mRNA Translation by MAPK Cascade During Mouse Oocyte Maturation. *Front. Cell Dev. Biol.* 8. doi:10.3389/fcell.2020.609430.
Cheng, S., and M. Schuh. 2024. Two mechanisms repress cyclin B1 translation to maintain prophase arrest in mouse oocytes. *Nat. Commun.* 15:10044. doi:10.1038/s41467-024-54161-w.
Church, D.L., K.L. Guan, and E.J. Lambie. 1995. Three genes of the MAP kinase cascade, mek-2, mpk-1/sur-1 and let-60 ras, are required for meiotic cell cycle progression in Caenorhabditis elegans. *Dev. Camb. Engl.* 121:2525–2535. doi:10.1242/dev.121.8.2525.
Colledge, W.H., M.B.L. Carlton, G.B. Udy, and M.J. Evans. 1994. Disruption of c-mos causes parthenogenetic development of unfertilized mouse eggs. *Nature*. 370:65–68. doi:10.1038/370065a0.
Conduit, P.T., A. Wainman, and J.W. Raff. 2015. Centrosome function and assembly in animal cells. *Nat. Rev. Mol. Cell Biol.* 16:611–624. doi:10.1038/nrm4062.
Conti, M., and C. Kunitomi. 2024. A genome-wide perspective of the maternal mRNA translation program during oocyte development. *Semin. Cell Dev. Biol.* 154:88–98. doi:10.1016/j.semcdb.2023.03.003.
Cox, J., and M. Mann. 2008. MaxQuant enables high peptide identification rates, individualized p.p.b.-range mass accuracies and proteome-wide protein quantification. *Nat. Biotechnol.* 26:1367–1372. doi:10.1038/nbt.1511.
Demichev, V., C.B. Messner, S.I. Vernardis, K.S. Lilley, and M. Ralser. 2020. DIA-NN: neural networks and interference correction enable deep proteome coverage in high throughput. *Nat. Methods*. 17:41–44. doi:10.1038/s41592-019-0638-x.
Dey, K.K., D. Xie, and M. Stephens. 2018. A new sequence logo plot to highlight enrichment and depletion. *BMC Bioinformatics*. 19:473. doi:10.1186/s12859-018-2489-3.
Dumollard, R., M. Levasseur, C. Hebras, P. Huitorel, M. Carroll, J.-P. Chambon, and A. McDougall. 2011. Mos limits the number of meiotic divisions in urochordate eggs. *Dev. Camb. Engl.* 138:885–895. doi:10.1242/dev.057133.
Dumont, J., M. Umbhauer, P. Rassinier, A. Hanauer, and M.-H. Verlhac. 2005. p90Rsk is not involved in cytostatic factor arrest in mouse oocytes. *J. Cell Biol.* 169:227–231. doi:10.1083/jcb.200501027.
Dupré, A., O. Haccard, and C. Jessus. 2010. Mos in the Oocyte: How to Use MAPK Independently of Growth Factors and Transcription to Control Meiotic Divisions. *J. Signal Transduct.* 2011:e350412. doi:10.1155/2011/350412.
Eliscovich, C., I. Peset, I. Vernos, and R. Méndez. 2008. Spindle-localized CPE-mediated translation controls meiotic chromosome segregation. *Nat. Cell Biol.* 10:858–865. doi:10.1038/ncb1746.
Field, C.M., and P. Lénárt. 2011. Bulk cytoplasmic actin and its functions in meiosis and mitosis. *Curr. Biol. CB*. 21:R825-830. doi:10.1016/j.cub.2011.07.043.
Fukasawa, K., and G.F. Vande Woude. 1995. Mos overexpression in Swiss 3T3 cells induces meiotic-like alterations of the mitotic spindle. *Proc. Natl. Acad. Sci. U. S. A.* 92:3430–3434.

883 doi:10.1073/pnas.92.8.3430.
884 Gerhart, J., M. Wu, and M. Kirschner. 1984. Cell cycle dynamics of an M-phase-specific cytoplasmic
885 factor in Xenopus laevis oocytes and eggs. *J. Cell Biol.* 98:1247–1255.
886 doi:10.1083/jcb.98.4.1247.
887 Gruneberg, U., R. Neef, X. Li, E.H.Y. Chan, R.B. Chalamalasetty, E.A. Nigg, and F.A. Barr. 2006. KIF14
888 and citron kinase act together to promote efficient cytokinesis. *J. Cell Biol.* 172:363–372.
889 doi:10.1083/jcb.200511061.
890 Halet, G., and J. Carroll. 2007. Rac activity is polarized and regulates meiotic spindle stability and
891 anchoring in mammalian oocytes. *Dev. Cell.* 12:309–317. doi:10.1016/j.devcel.2006.12.010.
892 Hashimoto, N., N. Watanabe, Y. Furuta, H. Tamemoto, N. Sagata, M. Yokoyama, K. Okazaki, M.
893 Nagayoshi, N. Takeda, and Y. Ikawa. 1994. Parthenogenetic activation of oocytes in c-mos-
894 deficient mice. *Nature*. 370:68–71. doi:10.1038/370068a0.
895 Heim, A., M.L. Niedermeier, F. Stengel, and T.U. Mayer. 2022. The translation regulator Zar1l
896 controls timing of meiosis in Xenopus oocytes. *Dev. Camb. Engl.* 149:dev200900.
897 doi:10.1242/dev.200900.
898 Hochegger, H., A. Klotzbücher, J. Kirk, M. Howell, K. le Guellec, K. Fletcher, T. Duncan, M. Sohail, and
899 T. Hunt. 2001. New B-type cyclin synthesis is required between meiosis I and II during
900 Xenopus oocyte maturation. *Dev. Camb. Engl.* 128:3795–3807.
901 doi:10.1242/dev.128.19.3795.
902 Hochstoeger, T., P. Papasaikas, E. Piskadlo, and J.A. Chao. 2024. Distinct roles of LARP1 and
903 4EBP1/2 in regulating translation and stability of 5'TOP mRNAs. *Sci. Adv.* 10:eadi7830.
904 doi:10.1126/sciadv.adi7830.
905 Hodgman, R., J. Tay, R. Mendez, and J.D. Richter. 2001. CPEB phosphorylation and cytoplasmic
906 polyadenylation are catalyzed by the kinase IAK1/Eg2 in maturing mouse oocytes. *Dev.*
907 *Camb. Engl.* 128:2815–2822. doi:10.1242/dev.128.14.2815.
908 Holubcová, Z., M. Blayney, K. Elder, and M. Schuh. 2015. Human oocytes. Error-prone chromosome-
909 mediated spindle assembly favors chromosome segregation defects in human oocytes.
910 *Science*. 348:1143–1147. doi:10.1126/science.aaa9529.
911 Hornbeck, P.V., B. Zhang, B. Murray, J.M. Kornhauser, V. Latham, and E. Skrzypek. 2015.
912 PhosphoSitePlus, 2014: mutations, PTMs and recalibrations. *Nucleic Acids Res.* 43:D512-
913 520. doi:10.1093/nar/gku1267.
914 Huerta-Cepas, J., D. Szklarczyk, K. Forslund, H. Cook, D. Heller, M.C. Walter, T. Rattei, D.R. Mende, S.
915 Sunagawa, M. Kuhn, L.J. Jensen, C. von Mering, and P. Bork. 2016. eggNOG 4.5: a hierarchical
916 orthology framework with improved functional annotations for eukaryotic, prokaryotic and
917 viral sequences. *Nucleic Acids Res.* 44:D286–D293. doi:10.1093/nar/gkv1248.
918 Hughes, C.S., S. Moggridge, T. Müller, P.H. Sorensen, G.B. Morin, and J. Krijgsveld. 2019. Single-pot,
919 solid-phase-enhanced sample preparation for proteomics experiments. *Nat. Protoc.* 14:68–
920 85. doi:10.1038/s41596-018-0082-x.
921 Huis In 't Veld, P.J., S. Wohlgemuth, C. Koerner, F. Müller, P. Janning, and A. Musacchio. 2022.
922 Reconstitution and use of highly active human CDK1:Cyclin-B:CKS1 complexes. *Protein Sci.*
923 *Publ. Protein Soc.* 31:528–537. doi:10.1002/pro.4233.
924 Humphrey, S.J., S.B. Azimifar, and M. Mann. 2015. High-throughput phosphoproteomics reveals in
925 vivo insulin signaling dynamics. *Nat. Biotechnol.* 33:990–995. doi:10.1038/nbt.3327.
926 Igea, A., and R. Méndez. 2010. Meiosis requires a translational positive loop where CPEB1 ensues its
927 replacement by CPEB4. *EMBO J.* 29:2182–2193. doi:10.1038/emboj.2010.111.
928 Ihaka, R., and R. Gentleman. 1996. R: A Language for Data Analysis and Graphics. *J. Comput. Graph.*
929 *Stat.* 5:299–314. doi:10.2307/1390807.
930 Ikeda, M., S. Chiba, K. Ohashi, and K. Mizuno. 2012. Furry Protein Promotes Aurora A-mediated
931 Polo-like Kinase 1 Activation. *J. Biol. Chem.* 287:27670–27681.
932 doi:10.1074/jbc.M112.378968.

933 Isoda, M., K. Sako, K. Suzuki, K. Nishino, N. Nakajo, M. Ohe, T. Ezaki, Y. Kanemori, D. Inoue, H. Ueno,
934 and N. Sagata. 2011. Dynamic Regulation of Emi2 by Emi2-Bound Cdk1/Plk1/CK1 and
935 PP2A-B56 in Meiotic Arrest of *Xenopus* Eggs. *Dev. Cell.* 21:506–519.
936 doi:10.1016/j.devcel.2011.06.029.
937 Ivanovska, I., E. Lee, K.M. Kwan, D.D. Fenger, and T.L. Orr-Weaver. 2004. The Drosophila MOS
938 ortholog is not essential for meiosis. *Curr. Biol. CB*. 14:75–80.
939 doi:10.1016/j.cub.2003.12.031.
940 Iwabuchi, M., K. Ohsumi, T.M. Yamamoto, W. Sawada, and T. Kishimoto. 2000. Residual Cdc2 activity
941 remaining at meiosis I exit is essential for meiotic M-M transition in Xenopus oocyte
942 extracts. *EMBO J.* 19:4513–4523. doi:10.1093/emboj/19.17.4513.
943 Jaffe, L.A., and M. Terasaki. 2004. Quantitative Microinjection of Oocytes, Eggs, and Embryos.
944 *Methods Cell Biol.* 74:219–242.
945 Jessus, C., C. Munro, and E. Houliston. 2020. Managing the Oocyte Meiotic Arrest-Lessons from Frogs
946 and Jellyfish. *Cells*. 9:1150. doi:10.3390/cells9051150.
947 Johnson, J.L., T.M. Yaron, E.M. Huntsman, A. Kerelsky, J. Song, A. Regev, T.-Y. Lin, K. Liberatore, D.M.
948 Cizin, B.M. Cohen, N. Vasan, Y. Ma, K. Krismer, J.T. Robles, B. van de Kooij, A.E. van
949 Vlimmeren, N. Andrée-Busch, N.F. Käufer, M.V. Dorovkov, A.G. Ryazanov, Y. Takagi, E.R.
950 Kastenhuber, M.D. Goncalves, B.D. Hopkins, O. Elemento, D.J. Taatjes, A. Maucuer, A.
951 Yamashita, A. Degterev, M. Uduman, J. Lu, S.D. Landry, B. Zhang, I. Cossentino, R. Linding, J.
952 Blenis, P.V. Hornbeck, B.E. Turk, M.B. Yaffe, and L.C. Cantley. 2023. An atlas of substrate
953 specificities for the human serine/threonine kinome. *Nature*. 613:759–766.
954 doi:10.1038/s41586-022-05575-3.
955 Keady, B.T., P. Kuo, S.E. Martínez, L. Yuan, and L.E. Hake. 2007. MAPK interacts with XGef and is
956 required for CPEB activation during meiosis in Xenopus oocytes. *J. Cell Sci.* 120:1093–1103.
957 doi:10.1242/jcs.03416.
958 Kudtarkar, P., and R.A. Cameron. 2017. Echinobase: an expanding resource for echinoderm genomic
959 information. *Database J. Biol. Databases Curation*. 2017:bax074.
960 doi:10.1093/database/bax074.
961 Lapasset, L., B. Pradet-Balade, J.-C. Lozano, G. Peaucellier, and A. Picard. 2005. Nuclear envelope
962 breakdown may deliver an inhibitor of protein phosphatase 1 which triggers cyclin B
963 translation in starfish oocytes. *Dev. Biol.* 285:200–210. doi:10.1016/j.ydbio.2005.06.016.
964 Lapasset, L., B. Pradet-Balade, V. Vergé, J.-C. Lozano, N. Oulhen, P. Cormier, and G. Peaucellier. 2008.
965 Cyclin B synthesis and rapamycin-sensitive regulation of protein synthesis during starfish
966 oocyte meiotic divisions. *Mol. Reprod. Dev.* 75:1617–1626. doi:10.1002/mrd.20905.
967 Lefebvre, C., M.E. Terret, A. Djiane, P. Rassinier, B. Maro, and M.-H. Verlhac. 2002. Meiotic spindle
968 stability depends on MAPK-interacting and spindle-stabilizing protein (MISS), a new MAPK
969 substrate. *J. Cell Biol.* 157:603–613. doi:10.1083/jcb.200202052.
970 Lénárt, P., and J. Ellenberg. 2003. Nuclear envelope dynamics in oocytes: from germinal vesicle
971 breakdown to mitosis. *Curr. Opin. Cell Biol.* 15:88–95. doi:10.1016/s0955-0674(02)00011-x.
972 Liu, J., P.D. Stevens, N.E. Eshleman, and T. Gao. 2013. Protein phosphatase PPM1G regulates protein
973 translation and cell growth by dephosphorylating 4E binding protein 1 (4E-BP1). *J. Biol.*
974 *Chem.* 288:23225–23233. doi:10.1074/jbc.M113.492371.
975 Lorenzo-Orts, L., M. Strobl, B. Steinmetz, F. Leesch, C. Pribitzer, J. Roehsner, M. Schutzbier, G.
976 Dürnberger, and A. Pauli. 2024. eIF4E1b is a non-canonical eIF4E protecting maternal
977 dormant mRNAs. *EMBO Rep.* 25:404–427. doi:10.1038/s44319-023-00006-4.
978 Mendez, R., L.E. Hake, T. Andresson, L.E. Littlepage, J.V. Ruderman, and J.D. Richter. 2000a.
979 Phosphorylation of CPE binding factor by Eg2 regulates translation of c-mos mRNA. *Nature*.
980 404:302–307. doi:10.1038/35005126.
981 Mendez, R., K.G. Murthy, K. Ryan, J.L. Manley, and J.D. Richter. 2000b. Phosphorylation of CPEB by
982 Eg2 mediates the recruitment of CPSF into an active cytoplasmic polyadenylation complex.

983 *Mol. Cell*. 6:1253–1259. doi:10.1016/s1097-2765(00)00121-0.
984 Mendez, R., and J.D. Richter. 2001. Translational control by CPEB: a means to the end. *Nat. Rev. Mol.*
985 *Cell Biol.* 2:521–529. doi:10.1038/35080081.
986 Minshall, N., M.H. Reiter, D. Weil, and N. Standart. 2007. CPEB interacts with an ovary-specific eIF4E
987 and 4E-T in early Xenopus oocytes. *J. Biol. Chem.* 282:37389–37401.
988 doi:10.1074/jbc.M704629200.
989 Mogessie, B., K. Scheffler, and M. Schuh. 2018. Assembly and Positioning of the Oocyte Meiotic
990 Spindle. *Annu. Rev. Cell Dev. Biol.* 34:381–403. doi:10.1146/annurev-cellbio-100616-
991 060553.
992 Mori, M., M. Hara, K. Tachibana, and T. Kishimoto. 2006. p90Rsk is required for G1 phase arrest in
993 unfertilized starfish eggs. *Dev. Camb. Engl.* 133:1823–1830. doi:10.1242/dev.02348.
994 Murtagh, F., and P. Legendre. 2014. Ward's Hierarchical Agglomerative Clustering Method: Which
995 Algorithms Implement Ward's Criterion? *J. Classif.* 31:274–295. doi:10.1007/s00357-014-
996 9161-z.
997 Ochi, H., S. Aoto, K. Tachibana, M. Hara, and K. Chiba. 2016. Block of CDK1-dependent polyadenosine
998 elongation of Cyclin B mRNA in metaphase-i-arrested starfish oocytes is released by
999 intracellular pH elevation upon spawning. *Mol. Reprod. Dev.* 83:79–87.
1000 doi:10.1002/mrd.22599.
1001 Oskarsson, M., W.L. McClements, D.G. Blair, J.V. Maizel, and G.F. Vande Woude. 1980. Properties of a
1002 normal mouse cell DNA sequence (sarc) homologous to the src sequence of Moloney
1003 sarcoma virus. *Science*. 207:1222–1224. doi:10.1126/science.6243788.
1004 Pal, D., A. Ellis, S.P. Sepúlveda-Ramírez, T. Salgado, I. Terrazas, G. Reyes, R. De La Rosa, J.H. Henson,
1005 and C.B. Shuster. 2020. Rac and Arp2/3-Nucleated Actin Networks Antagonize Rho During
1006 Mitotic and Meiotic Cleavages. *Front. Cell Dev. Biol.* 8:591141.
1007 doi:10.3389/fcell.2020.591141.
1008 Perez-Riverol, Y., J. Bai, C. Bandla, D. García-Seisdedos, S. Hewapathirana, S. Kamatchinathan, D.J.
1009 Kundu, A. Prakash, A. Frericks-Zipper, M. Eisenacher, M. Walzer, S. Wang, A. Brazma, and J.A.
1010 Vizcaíno. 2022. The PRIDE database resources in 2022: a hub for mass spectrometry-based
1011 proteomics evidences. *Nucleic Acids Res.* 50:D543–D552. doi:10.1093/nar/gkab1038.
1012 Phillips, K.P., M.A.F. Petrunewich, J.L. Collins, R.A. Booth, X.J. Liu, and J.M. Baltz. 2002. Inhibition of
1013 MEK or cdc2 Kinase Parthenogenetically Activates Mouse Eggs and Yields the Same
1014 Phenotypes as Mos−/− Parthenogenotes. *Dev. Biol.* 247:210–223.
1015 doi:10.1006/dbio.2002.0680.
1016 Piqué, M., J.M. López, S. Foissac, R. Guigó, and R. Méndez. 2008. A combinatorial code for CPE-
1017 mediated translational control. *Cell*. 132:434–448. doi:10.1016/j.cell.2007.12.038.
1018 Raudvere, U., L. Kolberg, I. Kuzmin, T. Arak, P. Adler, H. Peterson, and J. Vilo. 2019. g:Profiler: a web
1019 server for functional enrichment analysis and conversions of gene lists (2019 update).
1020 *Nucleic Acids Res.* 47:W191–W198. doi:10.1093/nar/gkz369.
1021 Richter, J.D., and P. Lasko. 2011. Translational control in oocyte development. *Cold Spring Harb.*
1022 *Perspect. Biol.* 3:a002758. doi:10.1101/cshperspect.a002758.
1023 Ritchie, M.E., B. Phipson, D. Wu, Y. Hu, C.W. Law, W. Shi, and G.K. Smyth. 2015. limma powers
1024 differential expression analyses for RNA-sequencing and microarray studies. *Nucleic Acids*
1025 *Res.* 43:e47. doi:10.1093/nar/gkv007.
1026 Sagata, N., M. Oskarsson, T. Copeland, J. Brumbaugh, and G.F.V. Woude. 1988. Function of c-mos
1027 proto-oncogene product in meiotic maturation in Xenopus oocytes. *Nature*. 335:519–525.
1028 doi:10.1038/335519a0.
1029 Samwer, M., H.-J. Dehne, F. Spira, M. Kollmar, D.W. Gerlich, H. Urlaub, and D. Görlich. 2013. The
1030 nuclear F-actin interactome of Xenopus oocytes reveals an actin-bundling kinesin that is
1031 essential for meiotic cytokinesis. *EMBO J.* 32:1886–1902. doi:10.1038/emboj.2013.108.
1032 Schindelin, J., I. Arganda-Carreras, E. Frise, V. Kaynig, M. Longair, T. Pietzsch, S. Preibisch, C. Rueden,

1033 S. Saalfeld, B. Schmid, J.-Y. Tinevez, D.J. White, V. Hartenstein, K. Eliceiri, P. Tomancak, and A.
1034 Cardona. 2012. Fiji: an open-source platform for biological-image analysis. *Nat. Methods*.
1035 9:676–682. doi:10.1038/nmeth.2019.
1036 Schuh, M., and J. Ellenberg. 2007. Self-organization of MTOCs replaces centrosome function during
1037 acentrosomal spindle assembly in live mouse oocytes. *Cell*. 130:484–498.
1038 doi:10.1016/j.cell.2007.06.025.
1039 Sensui, N., M. Yoshida, and K. Tachibana. 2012. Role of Mos/MEK/ERK cascade and Cdk1 in Ca2+
1040 oscillations in fertilized ascidian eggs. *Dev. Biol.* 367:208–215.
1041 doi:10.1016/j.ydbio.2012.05.011.
1042 Severson, A.F., G. von Dassow, and B. Bowerman. 2016. Oocyte Meiotic Spindle Assembly and
1043 Function. *Curr. Top. Dev. Biol.* 116:65–98. doi:10.1016/bs.ctdb.2015.11.031.
1044 Shakya, A., S. Park, N. Rana, and J.T. King. 2020. Liquid-Liquid Phase Separation of Histone Proteins
1045 in Cells: Role in Chromatin Organization. *Biophys. J.* 118:753–764.
1046 doi:10.1016/j.bpj.2019.12.022.
1047 Slep, K.C., and R.D. Vale. 2007. Structural Basis of Microtubule Plus End Tracking by XMAP215,
1048 CLIP-170 and EB1. *Mol. Cell*. 27:976–991. doi:10.1016/j.molcel.2007.07.023.
1049 Sluder, G., F.J. Miller, and K. Lewis. 1993. Centrosome inheritance in starfish zygotes. II: Selective
1050 suppression of the maternal centrosome during meiosis. *Dev. Biol.* 155:58–67.
1051 doi:10.1006/dbio.1993.1006.
1052 Standart, N., J. Minshull, J. Pines, and T. Hunt. 1987. Cyclin synthesis, modification and destruction
1053 during meiotic maturation of the starfish oocyte. *Dev. Biol.* 124:248–258.
1054 doi:10.1016/0012-1606(87)90476-3.
1055 Stebbins-Boaz, B., Q. Cao, C.H. de Moor, R. Mendez, and J.D. Richter. 1999. Maskin is a CPEB-
1056 associated factor that transiently interacts with elF-4E. *Mol. Cell*. 4:1017–1027.
1057 doi:10.1016/s1097-2765(00)80230-0.
1058 Strickland, L., G. von Dassow, J. Ellenberg, V. Foe, P. Lenart, and D. Burgess. 2004. Light microscopy
1059 of echinoderm embryos. *Methods Cell Biol.* 74:371–409. doi:10.1016/s0091-
1060 679x(04)74016-9.
1061 Swartz, S.Z., H.T. Nguyen, B.C. McEwan, M.E. Adamo, I.M. Cheeseman, and A.N. Kettenbach. 2021.
1062 Selective dephosphorylation by PP2A-B55 directs the meiosis I-meiosis II transition in
1063 oocytes. *eLife*. 10:e70588. doi:10.7554/eLife.70588.
1064 Tachibana, K., D. Tanaka, T. Isobe, and T. Kishimoto. 2000. c-Mos forces the mitotic cell cycle to
1065 undergo meiosis II to produce haploid gametes. *Proc. Natl. Acad. Sci.* 97:14301–14306.
1066 doi:10.1073/pnas.97.26.14301.
1067 Terret, M.E., C. Lefebvre, A. Djiane, P. Rassinier, J. Moreau, B. Maro, and M.-H. Verlhac. 2003. DOC1R:
1068 a MAP kinase substrate that control microtubule organization of metaphase II mouse
1069 oocytes. *Dev. Camb. Engl.* 130:5169–5177. doi:10.1242/dev.00731.
1070 Thom, G., N. Minshall, A. Git, J. Argasinska, and N. Standart. 2003. Role of cdc2 kinase
1071 phosphorylation and conserved N-terminal proteolysis motifs in cytoplasmic
1072 polyadenylation-element-binding protein (CPEB) complex dissociation and degradation.
1073 *Biochem. J.* 370:91–100. doi:10.1042/BJ20021462.
1074 Ucar, H., K. Tachibana, and T. Kishimoto. 2013. The Mos-MAPK pathway regulates Diaphanous-
1075 related formin activity to drive cleavage furrow closure during polar body extrusion in
1076 starfish oocytes. *J. Cell Sci.* 126:5153–5165. doi:10.1242/jcs.130476.
1077 Valdez, V.A., L. Neahring, S. Petry, and S. Dumont. 2023. Mechanisms underlying spindle assembly
1078 and robustness. *Nat. Rev. Mol. Cell Biol.* 1–20. doi:10.1038/s41580-023-00584-0.
1079 Verlhac, M.H., J.Z. Kubiak, M. Weber, G. Géraud, W.H. Colledge, M.J. Evans, and B. Maro. 1996. Mos is
1080 required for MAP kinase activation and is involved in microtubule organization during
1081 meiotic maturation in the mouse. *Dev. Camb. Engl.* 122:815–822.
1082 doi:10.1242/dev.122.3.815.

1083 Verlhac, M.H., C. Lefebvre, P. Guillaud, P. Rassinier, and B. Maro. 2000. Asymmetric division in
1084 mouse oocytes: with or without Mos. *Curr. Biol. CB*. 10:1303–1306. doi:10.1016/s0960-
1085 9822(00)00753-3.
1086 Wells, S.E., P.E. Hillner, R.D. Vale, and A.B. Sachs. 1998. Circularization of mRNA by eukaryotic
1087 translation initiation factors. *Mol. Cell*. 2:135–140. doi:10.1016/s1097-2765(00)80122-7.
1088 Wesolowska, N., I. Avilov, P. Machado, C. Geiss, H. Kondo, M. Mori, and P. Lenart. 2020. Actin
1089 assembly ruptures the nuclear envelope by prying the lamina away from nuclear pores and
1090 nuclear membranes in starfish oocytes. *eLife*. 9:e49774. doi:10.7554/eLife.49774.
1091 Wessel, G.M., A.M. Reich, and P.C. Klatsky. 2010. Use of Sea Stars to Study Basic Reproductive
1092 Processes. *Syst. Biol. Reprod. Med*. doi:10.3109/19396361003674879.
1093 Wu, J.Q., and S. Kornbluth. 2008. Across the meiotic divide - CSF activity in the post-Emi2/XErp1
1094 era. *J. Cell Sci.* 121:3509–3514. doi:10.1242/jcs.036855.
1095 Yang, F., W. Wang, M. Cetinbas, R.I. Sadreyev, and M.D. Blower. 2020. Genome-wide analysis
1096 identifies cis-acting elements regulating mRNA polyadenylation and translation during
1097 vertebrate oocyte maturation. *RNA N. Y. N.* 26:324–344. doi:10.1261/rna.073247.119.

Figure 1.

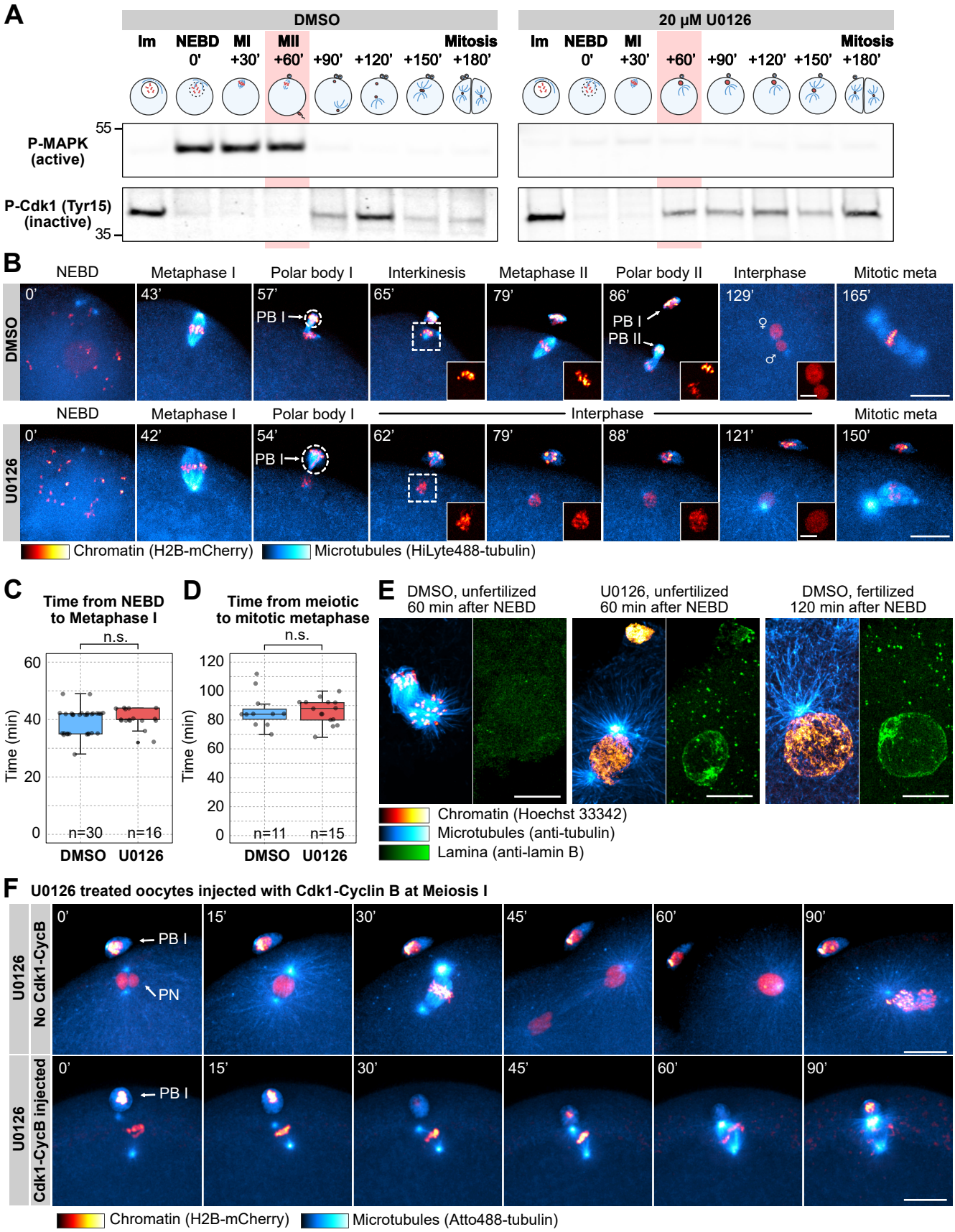
A
DMSO
20 μM U0126
Im
NEBD 0'
MI +30'
MII +60'
+90'
+120'
+150'
Mitosis +180'
P-MAPK (active)
P-Cdk1 (Tyr15) (inactive)
55
35
B
NEBD
Metaphase I
Polar body I
Interkinesis
Metaphase II
Polar body II
Interphase
Mitotic meta
DMSO
U0126
PB I
PB II
Chromatin (H2B-mCherry)
Microtubules (HiLyte488-tubulin)
C
Time from NEBD to Metaphase I
n.s.
Time (min)
n=30
n=16
DMSO
U0126
D
Time from meiotic to mitotic metaphase
n=11
n=15
E
DMSO, unfertilized 60 min after NEBD
U0126, unfertilized 60 min after NEBD
DMSO, fertilized 120 min after NEBD
Chromatin (Hoechst 33342)
Microtubules (anti-tubulin)
Lamina (anti-lamin B)
F
U0126 treated oocytes injected with Cdk1-Cyclin B at Meiosis I
U0126 No Cdk1-CycB
U0126 Cdk1-CycB injected
PB I
PN
Chromatin (H2B-mCherry)
Microtubules (Atto488-tubulin)

Figure 2.

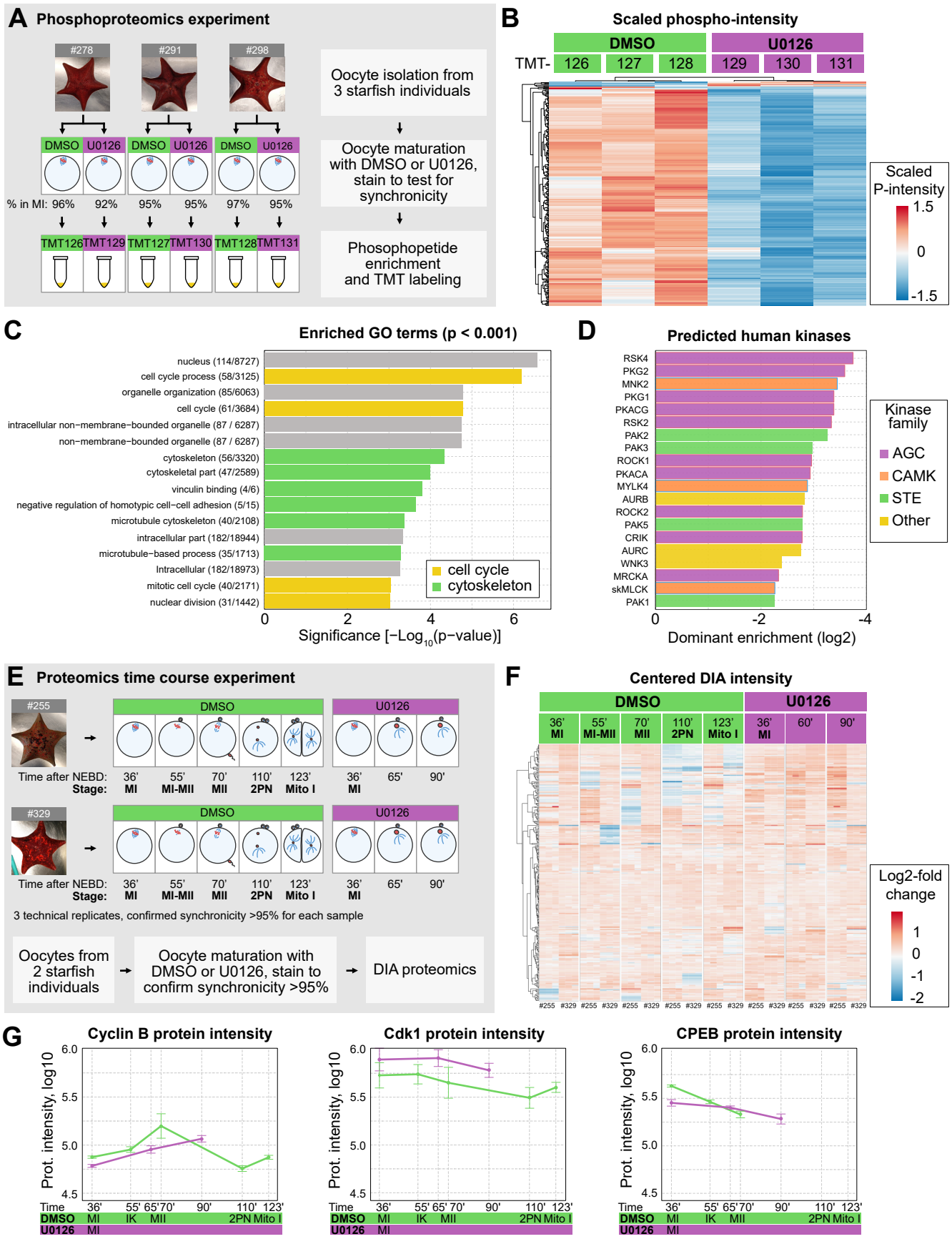
A Phosphoproteomics experiment
#278
#291
#298
DMSO U0126 DMSO U0126 DMSO U0126
% in MI: 96% 92% 95% 95% 97% 95%
TMT126 TMT129 TMT127 TMT130 TMT128 TMT131
Oocyte isolation from 3 starfish individuals
Oocyte maturation with DMSO or U0126, stain to test for synchronicity
Phosophopetide enrichment and TMT labeling
B Scaled phospho-intensity
DMSO
U0126
TMT- 126 127 128 129 130 131
Scaled P-intensity
1.5
0
-1.5
C Enriched GO terms (p < 0.001)
nucleus (114/8727)
cell cycle process (58/3125)
organelle organization (85/6063)
cell cycle (61/3684)
intracellular non−membrane−bounded organelle (87 / 6287)
non−membrane−bounded organelle (87 / 6287)
cytoskeleton (56/3320)
cytoskeletal part (47/2589)
vinculin binding (4/6)
negative regulation of homotypic cell−cell adhesion (5/15)
microtubule cytoskeleton (40/2108)
intracellular part (182/18944)
microtubule−based process (35/1713)
Intracellular (182/18973)
mitotic cell cycle (40/2171)
nuclear division (31/1442)
cell cycle
cytoskeleton
0 2 4 6
Significance [−Log10(p−value)]
D Predicted human kinases
RSK4
PKG2
MNK2
PKG1
PKACG
RSK2
PAK2
PAK3
ROCK1
PKACA
MYLK4
AURB
ROCK2
PAK5
CRIK
AURC
WNK3
MRCKA
skMLCK
PAK1
0 -2 -4
Dominant enrichment (log2)
Kinase family
AGC
CAMK
STE
Other
E Proteomics time course experiment
#255
#329
DMSO
U0126
Time after NEBD: 36' 55' 70' 110' 123' 36' 65' 90'
Stage: MI MI-MII MII 2PN Mito I MI
3 technical replicates, confirmed synchronicity >95% for each sample
Oocytes from 2 starfish individuals
Oocyte maturation with DMSO or U0126, stain to confirm synchronicity >95%
DIA proteomics
F Centered DIA intensity
DMSO
U0126
36' MI
55' MI-MII
70' MII
110' 2PN
123' Mito I
36' MI
60'
90'
Log2-fold change
1
0
-1
-2
G Cyclin B protein intensity
Cdk1 protein intensity
CPEB protein intensity
Prot. intensity, log10
6.0
5.5
5.0
4.5
Time 36' 55' 65' 70' 90' 110' 123'
DMSO MI IK MII 2PN Mito I
U0126 MI

Figure 3.

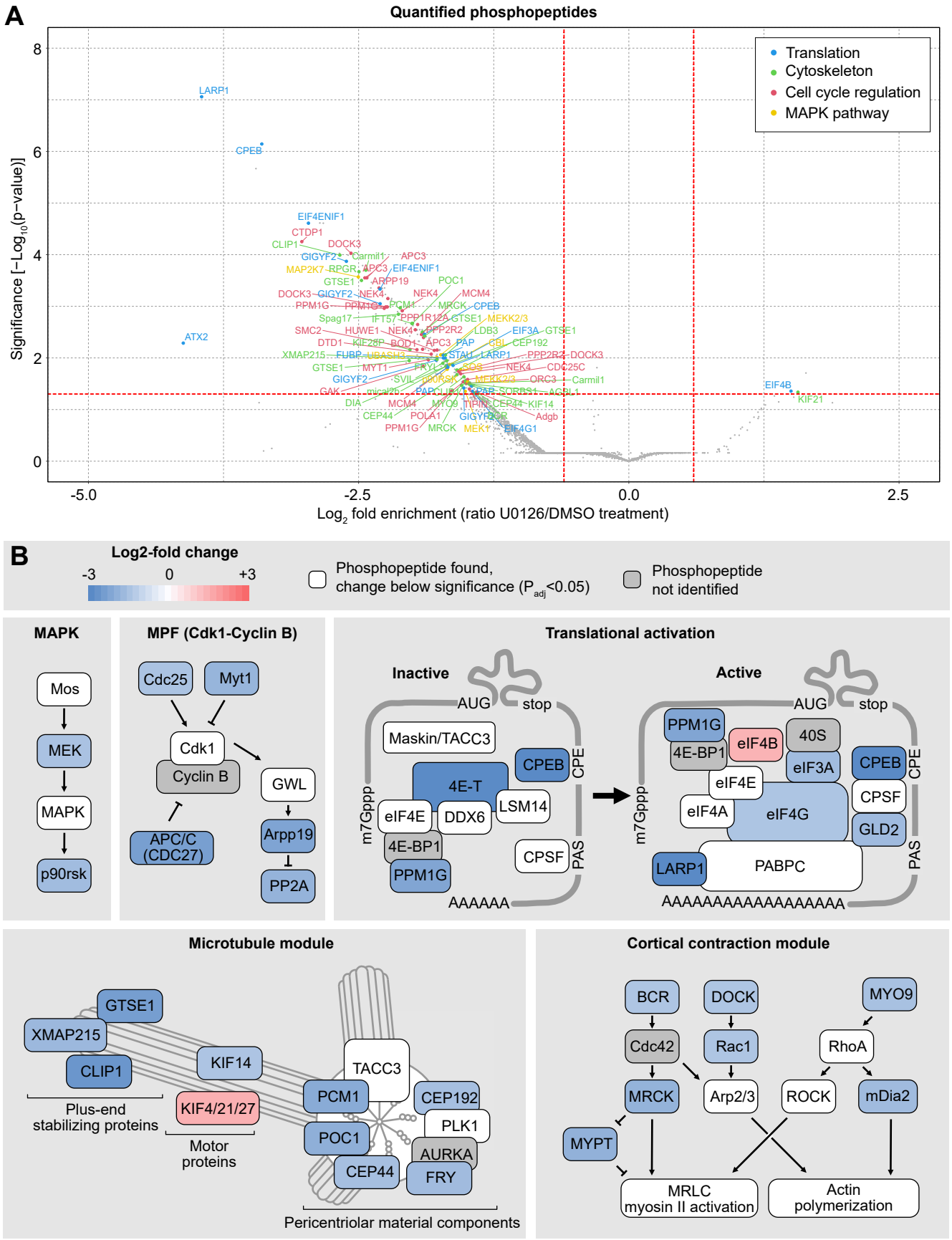
A
Quantified phosphopeptides
Translation
Cytoskeleton
Cell cycle regulation
MAPK pathway
Significance [−Log10(p−value)]
Log2 fold enrichment (ratio U0126/DMSO treatment)
B
Log2-fold change
-3
0
+3
Phosphopeptide found, change below significance (Padj<0.05)
Phosphopeptide not identified
MAPK
Mos
MEK
MAPK
p90rsk
MPF (Cdk1-Cyclin B)
Cdc25
Myt1
Cdk1
Cyclin B
GWL
Arpp19
PP2A
APC/C (CDC27)
Translational activation
Inactive
Active
AUG
stop
Maskin/TACC3
CPEB
CPE
4E-T
LSM14
DDX6
eIF4E
4E-BP1
PPM1G
CPSF
PAS
m7Gppp
AAAAAA
40S
eIF4B
eIF3A
eIF4A
eIF4G
GLD2
LARP1
PABPC
AAAAAAAAAAAAAAAAAA
Microtubule module
GTSE1
XMAP215
CLIP1
KIF14
KIF4/21/27
TACC3
PCM1
CEP192
PLK1
POC1
AURKA
CEP44
FRY
Plus-end stabilizing proteins
Motor proteins
Pericentriolar material components
Cortical contraction module
BCR
DOCK
MYO9
Cdc42
Rac1
RhoA
MRCK
Arp2/3
ROCK
mDia2
MYPT
MRLC myosin II activation
Actin polymerization

Figure 4.

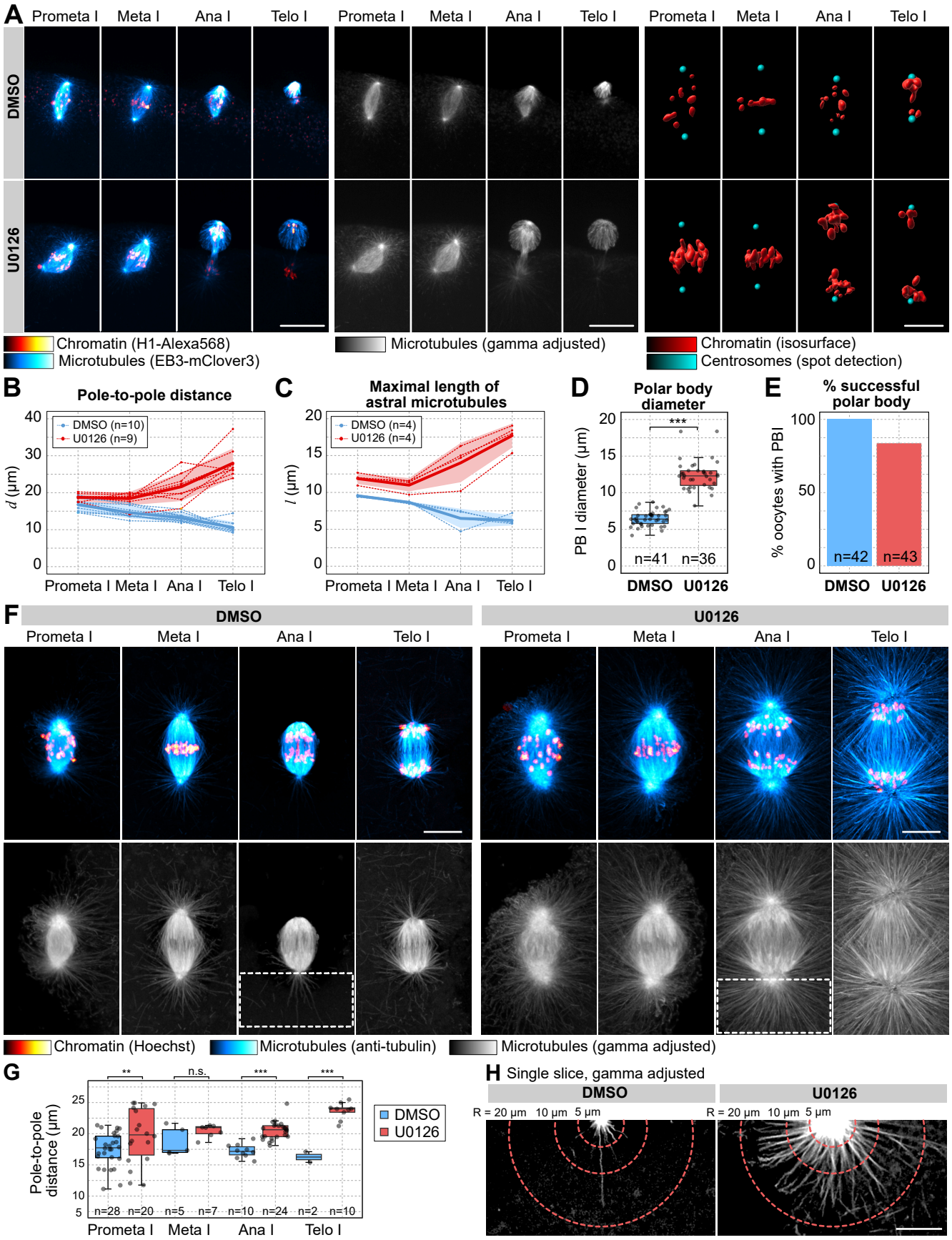
A
Prometa I
Meta I
Ana I
Telo I
DMSO
U0126
Chromatin (H1-Alexa568)
Microtubules (EB3-mClover3)
Microtubules (gamma adjusted)
Chromatin (isosurface)
Centrosomes (spot detection)
B
Pole-to-pole distance
DMSO (n=10)
U0126 (n=9)
d (µm)
C
Maximal length of astral microtubules
DMSO (n=4)
U0126 (n=4)
l (µm)
D
Polar body diameter
PB I diameter (µm)
***
n=41
n=36
E
% successful polar body
% oocytes with PBI
n=42
n=43
F
Chromatin (Hoechst)
Microtubules (anti-tubulin)
Microtubules (gamma adjusted)
G
Pole-to-pole distance (µm)
**
n.s.
***
n=28
n=20
n=5
n=7
n=10
n=24
n=2
n=10
H
Single slice, gamma adjusted
R = 20 µm
10 µm
5 µm

Figure 5.

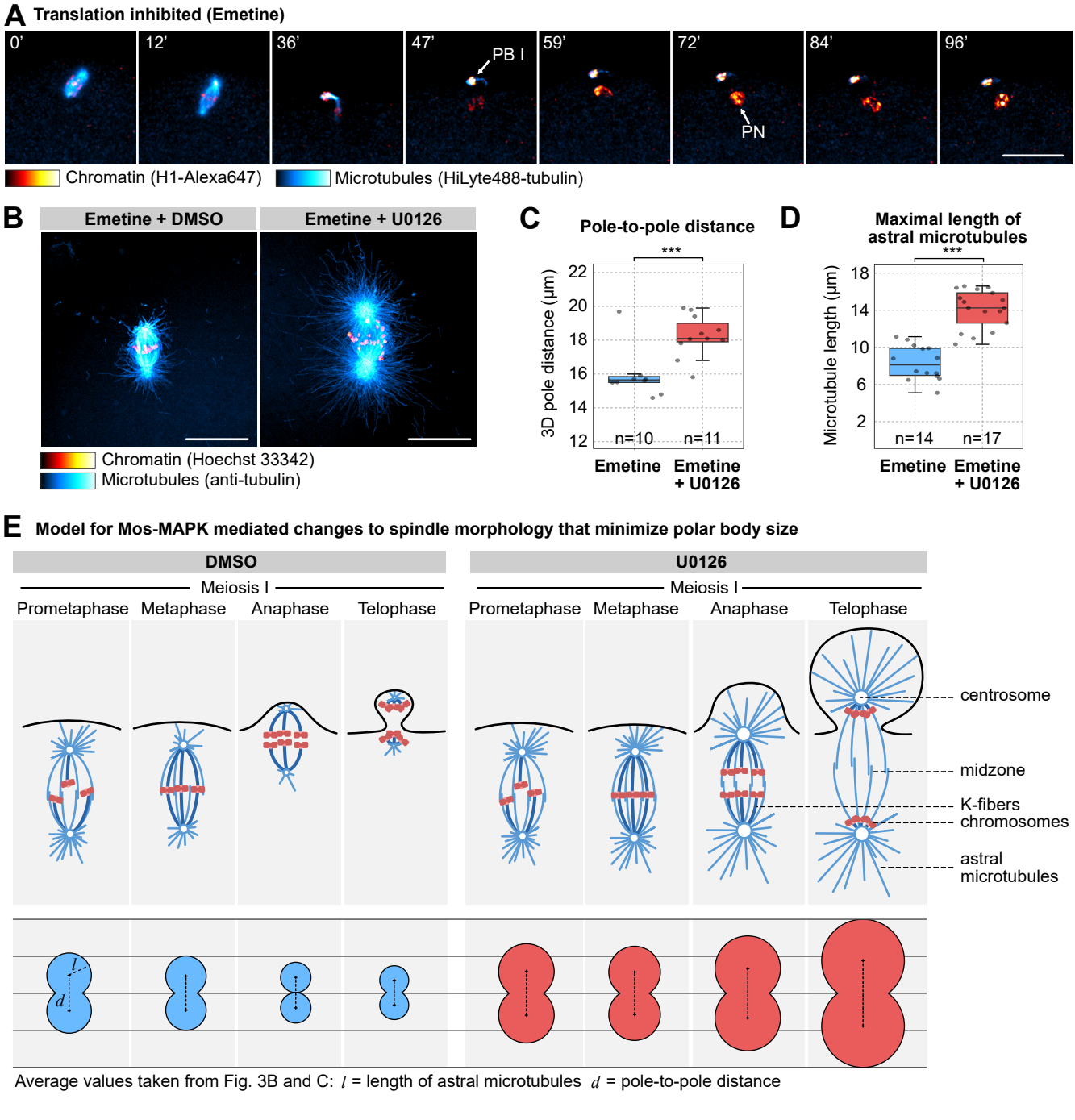

Average values taken from Fig. 3B and C: l = length of astral microtubules d = pole-to-pole distance